

Techno-Economic and Environmental Study of Grid-Connected Solar Geothermal Battery System in Tunisian Universities

Yassine Nefzi^{1*} , Hacem Dhahri² .

¹Department of Mechanical Engineering, College of Engineering, University of Gabes, 6029 Gabes, Tunisia .

²Thermal and Energetic Systems Studies Laboratory (LESTE), LR99ES31, College of Engineering, University of Monastir, 5000 Monastir, Tunisia.

E-mail: ¹yassine.nefzi@enig.rnu.tn, ²dhahri.hacem@gmail.com .

ARTICLE INFO.

Article history:

Received 3 Apr 2025

Received in revised form 5 Apr 2025

Accepted 3 June 2025

Available online 14 June 2025

KEYWORDS

solar–geothermal systems, thermal imbalance, energy modeling, policy, optimization, energy policy, multiobjective optimization.

ABSTRACT

This study aims to evaluate a hybrid energy system combining solar photovoltaic panels, ground-source heat pumps (GSHPs), and battery storage, within a unified university-based model applied to three distinct Tunisian climate zones: Beja, Gabes, and Borma. The methodology relied on a dynamic integration of OpenStudio and TRNSYS to accurately simulate annual thermal and electrical loads. A total of 35 design configurations per city were investigated, varying in borehole number and spacing, while system components were standardized to 1,137 photovoltaic panels rated at 450 W and 120 LiFePO₄ batteries with a storage capacity of 13.44 kWh.

Results revealed that the imbalance between cooling and heating demands leads to gradual thermal accumulation in the ground, reducing system efficiency over time. To assess mitigation strategies, a composite objective function incorporating four indicators was employed: thermal accumulation, ground field volume, instantaneous operating cost rate, and grid dependency. The optimization process identified configurations capable of limiting ground temperature rise and supporting stable operation. Sensitivity analysis showed that increasing the weight of economic and spatial indicators reshuffles the ranking of certain configurations, highlighting the importance of prioritization based on design goals. The selected configurations demonstrated the ability to cover more than 70% of annual demand, with levelized cost of energy (LCOE) ranging from 0.023 to 0.114 USD/kWh and payback periods between 23 and 44 years, depending on whether the system operates under Tunisia's restrictive grid policies or more supportive international frameworks.

*Corresponding author.

DOI: <https://doi.org/10.51646/jsesd.v14i1.516>

This is an open access article under the CC BY-NC license ([http://Attribution-NonCommercial 4.0 \(CC BY-NC 4.0\)](http://Attribution-NonCommercial 4.0 (CC BY-NC 4.0))).



Annual loads ranged from 965 to 1,135 MWh, with peak cooling reaching 660 kW and heating between 324 and 416 kW. Simulations also revealed seasonal variations in battery performance, with average daily charge levels exceeding 50–55% in July and dropping to 17–20% in January, depending on location. The study emphasizes the need to align technical configurations with regulatory reforms to ensure economic viability and accelerate the transition to sustainable energy systems in academic institutions.

دراسة تقنية اقتصادية بيئية لمنظومة الطاقة الشمسية طاقة جوف الارض البطاريات المرتبطة بالشبكة في الجامعات التونسية

ياسين نفزي، حسن ظاهري.

ملخص: تهدف هذه الدراسة إلى تقييم نظام طاقة هجين يجمع بين الألواح الشمسية، المضخات الجيوحرارية، وبطاريات التخزين، ضمن نموذج جامعي موحد يحاكي ثلاث مناطق مناخية تونسية: باجة، قابس، وبرمة. وقد اعتمدت المنهجية على تكامل ديناميكي بين OpenStudio و TRNSYS نمذجة الأحمال الحرارية والكهربائية السنوية بدقة عالية، شملت 35 توليفة تصميمية لكل مدينة، باختلاف عدد الآبار وتباعدها، مع اعتماد 1137 لوحًا شمسيًا بقدرة 450 واط لكل وحدة، و 120 بطارية من نوع LiFePO_4 بسعة 13.44 ك.و.س لكل واحدة، لتوحيد مكونات النظام عبر السيناريوهات. أظهرت النتائج أن اختلال التوازن بين أحمال التبريد والتدفئة يؤدي إلى تراكم حراري تدريجي في التربة، مما يضعف كفاءة النظام. ولتقييم الحلول الممكنة، تم اعتماد دالة هدف مركبة تضم أربعة مؤشرات: التراكم الحراري، حجم المجال الأرضي، الكلفة التشغيلية اللحظية، ونسبة الارتباط بشبكة الكهرباء الوطنية. وقد أفضت هذه العملية إلى تحديد تكوينات تقلل التراكم الحراري الأرضي وتُعد مرجعية للتشغيل المستقر. وقد بين تحليل الحساسية أن تعزيز وزن المؤشرات الاقتصادية والمساحية يعيد ترتيب بعض التكوينات التي كانت في مراكز متأخرة، مما يبرز أهمية ضبط الأوزان وفق أهداف التصميم. أظهرت هذه التكوينات قدرة على تغطية أكثر من 70% من الطلب السنوي، مع تراوح تكلفة الطاقة المستوية بين 0.023 و 0.114 دولار/ك.و.س، وأجال استرجاع استثمار تتراوح بين 23 و 44 سنة، وذلك بحسب ما إذا كان التشغيل خاضعًا للقيود التنظيمية المفروضة في تونس على بيع فائض الكهرباء، أو في ظل سياسات دولية مشجعة. وقد تراوحت الأحمال السنوية بين 965 و 1135 ميغاواط ساعة بحسب المناخ وتكوين النظام، مع بلوغ أقصى حمل تبريد 660 ك.و. والتدفئة بين 324 و 416 ك.و. كما كشفت المحاكاة عن تباين واضح في أداء البطاريات بين الفصول، حيث تجاوز متوسط الشحن اليومي 50–55% في يوليو، مقابل 17–20% فقط في يناير، بحسب الموقع الجغرافي. وتؤكد الدراسة على ضرورة الموازنة بين الخيارات التقنية مثل تحسين توزيع الآبار وتوسيع المجال الجوي والإصلاحات التنظيمية المحفزة، لضمان الجدوى الاقتصادية وتسريع الانتقال نحو أنظمة طاقة أكثر استدامة في المؤسسات التعليمية.

الكلمات المفتاحية – الأنظمة الطاقة الشمسية- طاقة جوف الارض، اختلال التوازن الحراري، نمذجة الطاقة، سياسات الطاقة، الامثلية، السياسة الطاقية، التحسين متعدد الأهداف.

1. INTRODUCTION

The economic and social advancement of modern societies is strongly tied to the reliable availability of energy. As a fundamental driver of industrial productivity, infrastructure development, and human welfare, energy plays a central role in shaping national trajectories. However, global energy production remains predominantly dependent on fossil fuels [1], which continue to accelerate climate change, environmental degradation, and resource depletion [2]. In response, a worldwide transition toward renewable and sustainable energy technologies has emerged as an urgent imperative. Driven by concerns about climate change and global warming, the global installed capacity of renewable energy grew by 50% in 2023. By the end of 2023, the global installed capacities of renewables such as solar, wind, hydropower, geothermal, marine, and biogas reached about 3.372 terawatts (TW), including 1.6 TW for PV solar energy systems

and 16.335 gigawatts (GW) for geothermal [3]. This growth reflects a profound global shift toward clean and sustainable energy solutions, particularly in the building sector, which is responsible for 28% of global CO₂ emissions and nearly 40% of total primary energy consumption in developed countries [4]. Given that urban populations are projected to rise from 55% today to 68% by 2050, improving energy performance in buildings has become a key pillar of sustainable development [5]. Efforts now focus on reducing energy consumption and emissions through passive design, high-efficiency systems, and on-site renewable integration [6]. Among these strategies, hybrid renewable energy systems that combine PV with geothermal sources have gained particular attention. These systems balance the intermittency of solar energy with the thermal stability of ground source heat pumps, offering year-round reliability [7]. For instance, D'Agostino et al. [8] showed that integrating PV with GSHPs can reduce primary energy use by up to 55% and CO₂ emissions by 67%, especially in cold climates. Moreover, techno-economic assessments highlight the synergy between technological innovation and policy support. A U.S.-based study on net-zero energy buildings (NZEBs) emphasized that improving PV efficiency can shorten payback periods more significantly than carbon pricing measures alone [9]. This suggests that the convergence of technical performance and institutional incentives is critical to accelerating the adoption of such systems [10]. While numerous studies have investigated the integration of solar and geothermal systems in residential and commercial buildings across Europe and North America, limited research has focused on the applicability and performance of such hybrid configurations in North African contexts—particularly within university infrastructure. This regional gap is critical, as higher education institutions are both high energy consumers and potential models for sustainable transformation. Addressing this gap, the present study examines the energy performance and environmental implications of solar-geothermal systems in university buildings, aiming to provide a replicable framework for similar institutions across arid and semi-arid regions. Against this backdrop, the present study investigates advanced configurations that combine photovoltaic and geothermal technologies to support sustainable energy transitions in the building sector. It aims to assess their performance and feasibility in North African climates, using simulation tools to explore their potential for reducing energy consumption and environmental impact in higher education buildings.

2. Literature Review

2.1. Hybrid Renewable Energy Systems (HRES)

Hybrid Renewable Energy Systems (HRES) offer effective solutions for meeting increasing energy demands, particularly in regions with infrastructure limitations or unstable supply. These systems combine two or more renewable sources—such as solar, wind, biomass, or geothermal—along with storage or backup units to enhance reliability and performance [11].

Recent studies from Libya and Gaza have evaluated hybrid PV-biogas systems adapted to daily residential demands of approximately 1,074 kWh, with peak loads reaching 84.5 kWp. Simulations conducted using HOMER Pro and performance metrics based on IEC 61724 demonstrated strong technical and economic viability [12][13]. On a national scale, an integrated assessment in Palestine using SAM and HOMER revealed that well-designed hybrid systems could supply up to 82% of the annual electricity demand while exporting surplus energy to the grid [14]. In the industrial sector, a grid-connected PV system deployed at a soap manufacturing facility in Rwanda achieved a 50% reduction in electricity costs and an expected profit of \$768,000 over 30 years, with a payback period of 10 years [15]. A hybrid PV-wind-diesel system installed at a quarantine center in Gaza also proved highly efficient, reducing the cost of energy by 54.89% compared to diesel-only configurations [16]. Advanced control strategies, such as the Whale

Optimization Algorithm (WOA), have further improved microgrid performance by optimizing sizing and operation of PV-wind-battery systems, achieving a LCOE as low as \$0.01/kWh and an LPSP of just 0.08% [17]. From a long-term planning perspective, energy modeling in Ghana using the IAEA's MESSAGE tool showed that a diversified energy mix could reduce carbon emissions by 55.27% and energy costs by 32.3% by 2048 [18]. Nonetheless, other studies have emphasized ongoing challenges such as inadequate financing, weak regulatory frameworks, and limited smart grid infrastructure [19][20]. These findings reinforce the importance of designing hybrid systems tailored to local resource availability, climatic conditions, and economic constraints, particularly in North African contexts such as Tunisia.

2.2. Geothermal Heat Pumps and Their Integration in HRES

In this context, geothermal and solar-assisted heat pumps are gaining traction as core components of hybrid systems. Heat pumps offer an efficient alternative to conventional boilers in both new and renovated buildings, contributing to the achievement of European directive targets. According to directive 2009/28/EC, aerothermal, geothermal, and hydrothermal sources are classified as renewable energy sources [21]. While air-source heat pumps are widely used, their performance fluctuates with ambient air temperature. By contrast, geothermal heat pumps (GHPs) benefit from the year-round thermal stability of the ground, ensuring more consistent and efficient operation [22]. Below a depth of approximately 10 meters, soil and groundwater temperatures exhibit minimal seasonal variation, depending on soil composition and moisture content. Ground Source Heat Pump (GSHP) systems consequently achieve high Coefficients of Performance (COP), lower energy consumption, and environmentally friendly operation, making them ideal for both public and residential buildings [23]. Understanding subsurface thermal dynamics is thus essential. Under Tunisian conditions, Boughanmi et al. [24] observed that at a depth of 3 meters, soil temperature remains relatively stable during summer, ranging between 27.5°C and 20°C., while Allouhi [25] proposed an integrated power-to-heat system coupling surplus PV electricity with open-loop GHPs. Similarly, Rodríguez Alejandro et al. [26] conducted experimental and numerical investigations on a vertical GHP in Mexico, analyzing its behavior under real climate conditions and applying CFD and thermoeconomic modeling to allocate costs across system components.

To further improve heat transfer in ground exchangers, Saeidi et al. [27] proposed novel designs that achieved a 37% increase in exchanger efficiency and a 3.8% drop in outlet fluid temperature in cooling mode. Mahmoud Fouad [28] also assessed the performance of GSHPs in hot, arid climates for residential cooling applications. In parallel, Acar and Kaska [29] studied solar-assisted ground-source heat pump systems with various solar collectors, revealing the value of hybridizing solar and geothermal sources to optimize energy use. Urban deployment strategies were addressed by Ramos-Escudero et al. [30], who developed a spatial optimization tool to facilitate GSHP adoption in densely built environments. Salhein et al. [31] further demonstrated that appropriate borehole spacing minimizes thermal interference and ensures long-term operational efficiency. Collectively, these advances underscore the growing viability of GSHPs as a key pillar in renewable hybrid heating and cooling strategies.

2.3. Battery Storage Systems in HRES

Battery storage plays a pivotal role in enhancing the autonomy and stability of HRES. Integrating solar and other renewable sources into buildings supports grid independence and emission reductions [32]. The rapid advancement in battery technologies has driven growing interest in evaluating the feasibility of renewable systems supported by electrical storage, particularly for building applications [33]. Research confirms that batteries are a practical solution—especially

in off-grid areas—for improving the exploitation of renewable energy [34]. As technology has matured, energy storage systems have become increasingly widespread in both residential and industrial sectors [35]. Liu et al. developed a system combining PVT modules, heat pumps, and thermoelectric generators, where battery storage mitigated solar radiation variability [36]. Silva et al., assessing an off-grid Amazonian town, showed that batteries were more cost-effective than hydrogen storage [37]. Conversely, Behzadi and Arabkoohsar raised concerns about the reliability of two-generation systems without storage [38]. Several comparative studies—such as that of Wang et al.—have demonstrated battery superiority over ice or PCM-based storage in terms of energy savings [39]. In Greece, a PV-diesel-battery system achieved a renewable penetration rate of 41.7% for a laboratory building [40], while Zhang et al. demonstrated the cost-effectiveness of battery storage over hydrogen in Sweden [41]. Further studies by Ozcan et al. [42] and Boruah & Chandel [43] explored performance optimization under diverse conditions to improve grid resilience. Zhang et al. [44] designed a zero-energy building powered by a diesel-solar-battery mix. Hemmati [45] proposed a mobile battery swapping station that reduced system costs by 5% compared to stationary setups. Innovative battery chemistries were also explored. Wang et al. [46] utilized zinc-ion batteries for direct solar storage, and Li [47] optimized PV-battery setups for Australian households, achieving \$2,500 annual savings with a 6.1 kWh battery. Schram et al. [48] analyzed Dutch homes, identifying optimal battery sizes between 0.5 and 9 kWh based on usage patterns. Finally, Talent and Du [49] optimized PV-battery sizing strategies for various tariff regimes, maximizing net present value for buildings of different scales.

3. Contribution of the recent study

This study presents a significant contribution to the field of hybrid renewable energy systems (HRES) by conducting a comprehensive multi-climatic evaluation of a system integrating photovoltaic panels, geothermal heat pumps with vertical borehole fields, and battery storage. While prior studies have assessed the influence of climate variability on renewable system performance [50], and others have focused on design-related parameters [51], few have systematically combined both climatic and design dimensions within a unified dynamic simulation framework. To address this gap, a standardized university building model was developed in OpenStudio and EnergyPlus to generate annual thermal and electrical loads. This was coupled with a TRNSYS platform to simulate full system dynamics, including electric control, heating, and hot water subsystems. The study evaluates 35 configurations per city (Beja, Gabes, Borma), generated from seven borehole quantities and five spacing values, enabling detailed exploration of the interaction between climatic variability and geothermal field design. The simulation incorporates battery storage operation based on production–demand balance, dynamic control of the number of active heat pumps based on real-time demand, and hot water production based on solar availability with auxiliary heating support when needed. System performance is evaluated in terms of actual energy demand, grid dependency, operating cost, carbon emissions, and supply reliability.

The main contributions of this study are:

- A parametric comparison of 35 design configurations per city, assessing the combined effects of borefield layout and climatic conditions.
- A unified simulation workflow integrating OpenStudio/EnergyPlus for building load modeling and TRNSYS for system-level dynamic analysis.
- A multi-objective evaluation framework based on normalized indicators—soil temperature rise, borefield footprint, instantaneous cost rate, and share of clean energy—with a weighted scoring method for ranking alternatives.
- Integration of exclusion criteria to eliminate thermally unstable configurations (e.g., excessive long-term ground temperature increase), ensuring the technical feasibility of selected solutions.

- Incorporation of extended economic and environmental metrics, including two formulations of levelized cost of energy (LCOE) and payback time (PBTM), both reflecting the influence of national energy policies; the cost of environmental damage from grid dependency; and a sensitivity analysis on indicator weights to assess the robustness of configuration rankings.

4. System description

4.1. General system overview

The proposed HRES's primary goal is to supply electricity to the on-grid building and store any excess electricity in the battery. The transiently simulated proposed system utilizes two types of photovoltaic panels—roof and green space panels—as energy generators, along with a battery bank, heat pump, evacuated tube collector, auxiliary heater, and hot water tank. Furthermore, this system employs three types of controllers: a power controller, an HVAC controller, and a hot water system controller, all of which monitor system performance. A comprehensive illustration of the system layout, including the arrangement of all components, is provided in Figure 1, facilitating an understanding of the system's structure and operation.

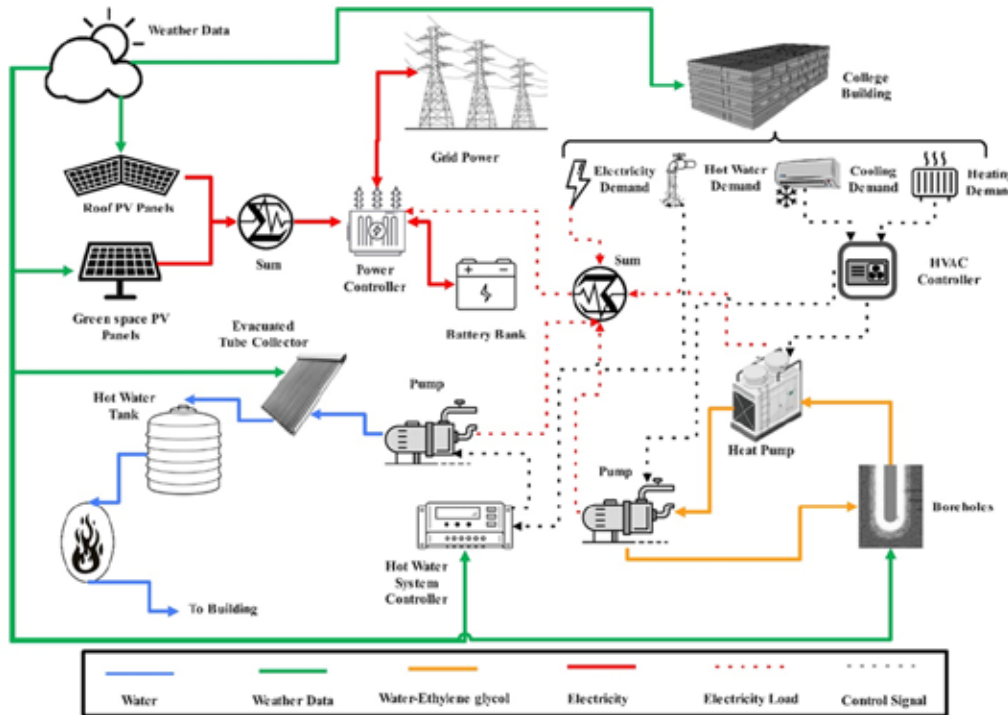


Figure 1. Schematic representation of the suggested system for the near-zero energy building.

4.2. Energy flow management and control strategy

OpenStudio-EnergyPlus calculates the building's thermal load and transfers the data to TRNSYS. Photovoltaic (PV) panels generate electricity based on hourly meteorological data. The system controller evaluates whether the generated energy exceeds demand, leading to two possible scenarios:

- **Surplus Energy Scenario:** If energy production exceeds demand, the excess electricity is stored in the battery. If the battery reaches its capacity limit, the surplus energy is exported to the grid.
- **Deficit Energy Scenario:** If the generated renewable energy is insufficient to meet the building's demand, the system first utilizes stored energy in the battery. If both stored and generated energy

are inadequate, the required electricity is drawn from the grid.

This control logic is illustrated in Figure 2-a, which presents a flowchart simplifying the energy dispatch strategy across PV production, battery, and grid resources. The diagram enhances clarity by visually representing the system’s decision-making under surplus and deficit scenarios. Within the TRNSYS framework, this logic is executed by the inverter component, which coordinates energy flows among system elements under varying load conditions.

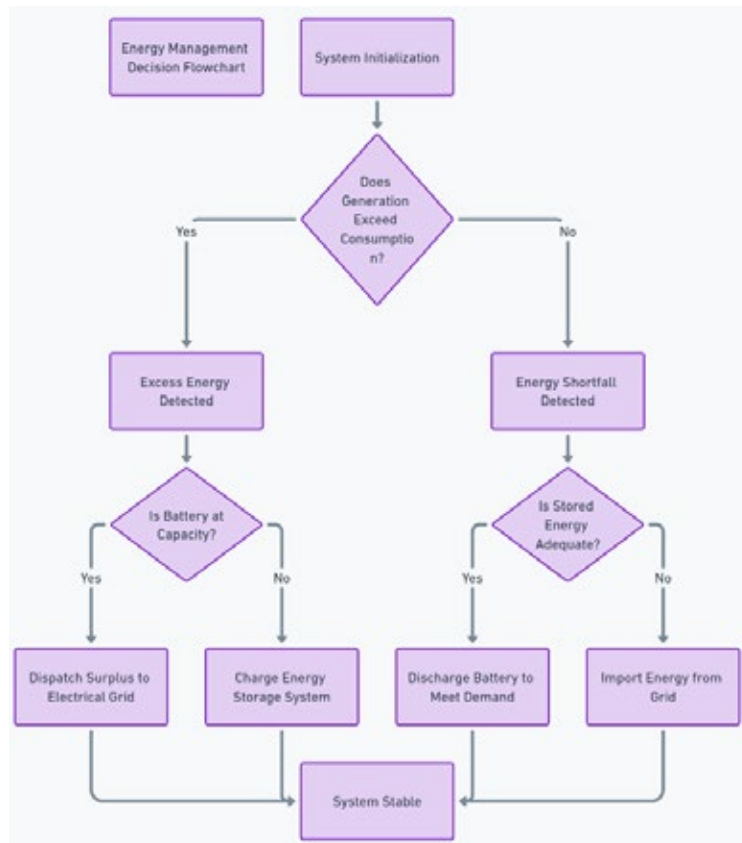


Figure 2-a. Energy management flow diagram.

4.3. Domestic hot water supply and control strategy

The domestic hot water (DHW) supply is primarily provided by an evacuated solar collector, with an auxiliary heater serving as a backup when solar energy is insufficient. The system includes a storage tank and a pump to ensure efficient hot water distribution. The pump operation follows a control logic based on two independent conditions: sufficient solar radiation or a demand for hot water in the building. The control signal is defined as follows:

$$Pump_{Signal} = \min(GT(Rad, 100) + GT(V_{DHW}, 1), 1) \quad (1)$$

where:

- Rad (W/m^2) represents the incident solar radiation on the collector, with a threshold of $100 W/m^2$, ensuring effective solar heating under typical operating conditions.
- V_{DHW} (L) represents the domestic hot water demand in the building, ensuring that the pump is activated only when demand exceeds 1 liter, preventing unnecessary activation for minimal consumption.
- $GT(x, y)$ is a comparator function that returns 1 if $x > y$, otherwise 0.

This logic ensures that the pump is activated when either solar radiation exceeds $100 W/m^2$ or there is a measurable hot water demand, without requiring both conditions to occur simultaneously.

The min function ensures that the control signal does not exceed 1. This strategy prioritizes solar energy utilization while ensuring a continuous hot water supply by activating the pump only when necessary.

To enhance the understanding of this control logic, Figure 2-b illustrates the decision-making flow for activating the pump, selecting solar or auxiliary heating, and ensuring a continuous domestic hot water supply.

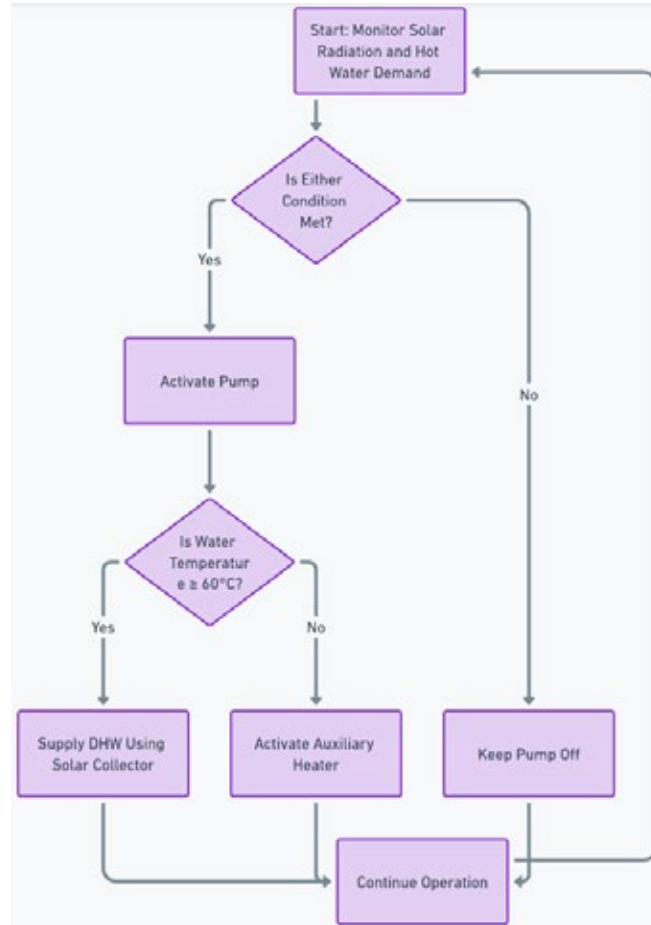


Figure 2-b. Flowchart of DHW Control Logic.

Specifications of the auxiliary heater referenced in the flowchart are listed below.

Table 1. Technical characteristics of the auxiliary fluid heater [52].

Parameters	Value	Unit
Auxiliary Fluid Heater		
Type	138	-
Maximum heating rate	50000	kJ/hr
Efficiency of auxiliary heater	95	%
Set point temperature	60	°C
Specific heat of fluid	4.19	kJ/kg. K

4.4. Heat pump sizing and dynamic control strategy

EnergyPlus simulations provide precise data on the building’s heating and cooling loads, enabling an optimized heat pump sizing strategy. The objective is to meet peak loads without oversizing the system, thereby reducing operational costs. Heating and cooling control signals are determined

as follows:

$$C_{heat} = GT(Q_{heat}, 0) \tag{2}$$

$$C_{cool} = GT(Q_{cool}, 0) \tag{3}$$

where:

- Q_{heat} and Q_{cool} (kJ/hr) represent the hourly heating and cooling loads, respectively.
- $GT(a, b)$ is a logical function that returns 1 if $a > b$, ensuring that the heat pump operates only when needed.

The predefined cooling and heating capacities for a single heat pump are 143,000 kJ/hr and 148,500 kJ/hr, respectively, with a maximum operational limit of 16 heat pumps. The HVAC system dynamically adjusts the number of active heat pumps based on real-time demand, ensuring optimal energy efficiency.

Calculation of the Required Number of Heat Pumps:

$$N_c = \frac{Q_{cool}}{Cap_{cool}} \tag{4}$$

$$N_h = \frac{Q_{heat}}{Cap_{heat}} \tag{5}$$

where:

- Cap_{cool} and Cap_{heat} (kJ/hr) are the predefined cooling and heating capacities of a single heat pump.
- N_c and N_h represent the theoretical number of heat pumps required to meet the building's hourly cooling and heating loads, respectively.

Since only full units of heat pumps can be operated, the decimal fraction is removed using the modulo function:

$$N_{c,eff} = N_c - mod(N_c, 1) \tag{6}$$

$$N_{h,eff} = N_h - mod(N_h, 1) \tag{7}$$

where:

- $N_{c,eff}$ and $N_{h,eff}$ are the effective integer values of required heat pumps after rounding down.
- $mod(x, 1)$ extracts the fractional part of x , ensuring only full heat pump units are considered.

Activation of Heat Pumps Based on Demand:

$$N_{c,act} = C_{cool} \times N_{c,eff} \tag{8}$$

$$N_{h,act} = C_{heat} \times N_{h,eff} \tag{9}$$

- $N_{c,act}$ and $N_{h,act}$ represent the number of heat pumps actively engaged in cooling and heating, respectively.
- C_{cool} and C_{heat} are control signals that determine whether heat pumps should be activated based on the presence of a cooling or heating load.

Determination of the Final Number of Operating Heat Pumps:

$$N_{hp} = min(N_{max}, N_{c,act} + N_{h,act}) \tag{10}$$

where:

- N_{max} presents the maximum allowable number of heat pumps (16 units).
- The min function ensures that the total number of operating heat pumps never exceeds the system's upper limit.

This approach enables a dynamic response to fluctuating thermal loads, thereby enhancing the operational efficiency of heat pumps and reducing operating costs by adjusting the number of

active units according to actual demand. Moreover, leveraging TRNSYS's built-in equation-solving environment eliminates the need to manually program models using general-purpose platforms such as MATLAB or Python. This simplifies the simulation workflow and enhances model integration within a framework specifically tailored to thermal and energy systems. This dynamic control sequence is summarized in Figure 2-c, which outlines the decision-making path for detecting loads, computing units, and enforcing the system's upper limit of 16 heat pumps.

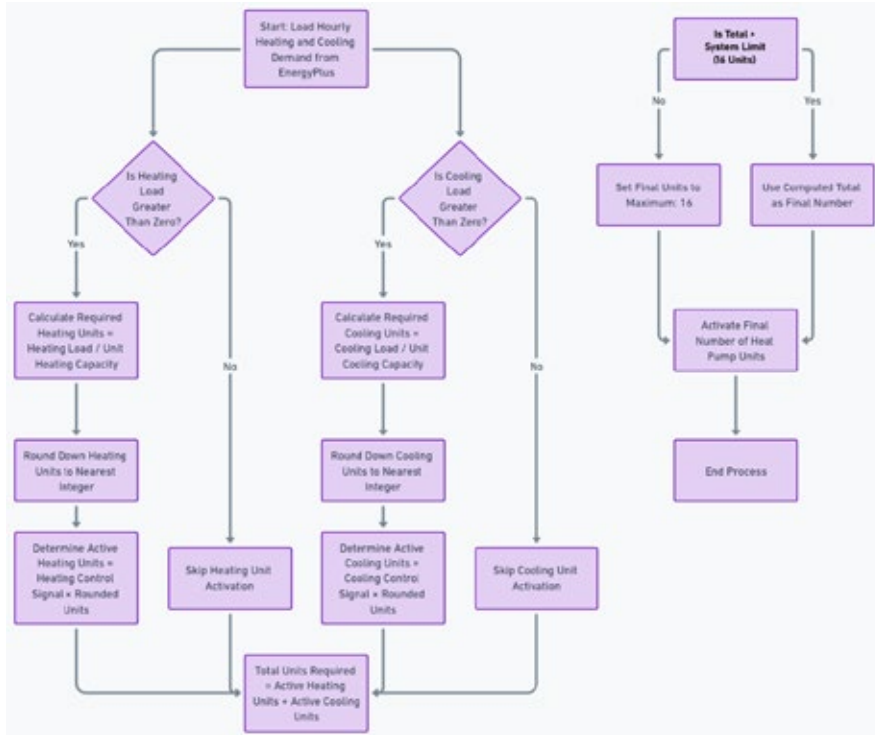


Figure 2-c. Flowchart of dynamic heat pump activation and capacity control.

Listed below are parameters governing heat pump unit selection.

Table 2. The heat pump's technical characteristics [53].

Parameters	Value	Unit
Type	927	-
Logical Unit Number for Cooling Data File	48	-
Number of Source Temperatures - Cooling	8	-
Number of Load Temperatures - Cooling	4	-
Logical Unit for Heating Data	49	-
Number of Source Temperatures - Heating	6	-
Number of Load Temperatures - Heating	4	-
Number of Source Flow rates	3	-
Number of Load Flow rates	3	-
Rated Cooling Power per Heat Pump	24869	kJ/hr
Rated Heating Power per Heat Pump	39079	kJ/hr
Inlet Source Temperature	10	°C
Source Flowrate	7722	kg/hr
Inlet Load Temperature	20.0	°C
Load Flowrate	1440.0	kg/hr

4.4.1. Maximum Units Justification

A probabilistic approach was adopted to define the system's upper design limit of 16 heat pump units.

As shown in Figure 3, the sorted hourly thermal demand profiles over 8,760 hours reveal that only the top 2% of hours (~175 hours) exceed this capacity.

The convergence of the demand curves across all cities below this threshold supports a unified design criterion. This sizing method avoids oversizing based on absolute peaks and ensures a balance between reliability, economic viability, and system efficiency.

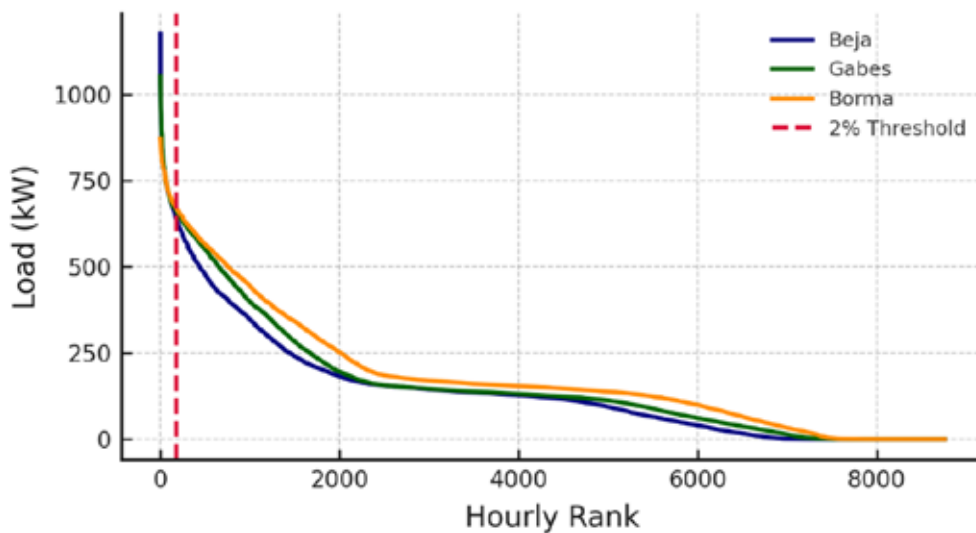


Figure 3. Sorted Thermal Loads with 2% Exceedance and Unified Design Limit.

5. Methodology

The methodological approach adopted in this study integrates building energy simulation, solar-geothermal system design, and performance evaluation under varying climatic conditions.

It begins with modeling the architectural and thermal characteristics of the case-study building and incorporating site-specific meteorological data.

The next stage involves the design and simulation of the electrical subsystem, including photovoltaic panel placement and battery storage modeling, to ensure optimal solar utilization and energy autonomy under spatial and shading constraints.

This is followed by the configuration of the geothermal borehole field based on thermal properties and site geometry. A detailed techno-economic and environmental assessment is then carried out to evaluate system performance across multiple configurations.

Finally, the analysis includes a critical discussion of modeling assumptions, limitations, and sources of uncertainty, which ultimately leads to a multi-objective optimization stage for selecting the optimal hybrid system configuration.

The overall simulation workflow—ranging from SketchUp-based geometry modeling to OpenStudio–EnergyPlus integration and TRNSYS-based dynamic simulation—is summarized in Figure 4.

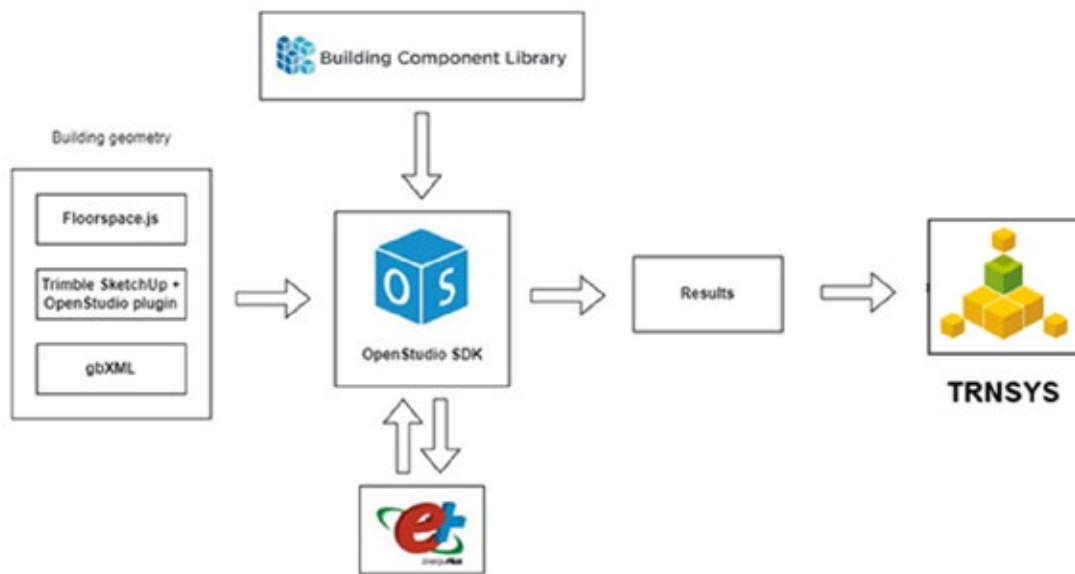


Figure 4. Energy Simulation Workflow Using OpenStudio and TRNSYS.

5.1. Building and Climate Setup

The college building spans 6,415 m², with a roof area of 1,660 m², and consists of four floors. The ground floor includes a multi-purpose study lounge, a boardroom, two lecture theaters, and a media complex, along with nine faculty offices, restrooms for staff and students, a storeroom, a utility room, a main entrance, a public elevator, and both main and secondary staircases. The second and third floors share identical layouts, each containing eight classrooms, a conference room, nine offices, and two studios, along with restrooms for faculty and students, utility rooms, and corridors—two on the third floor and one on the second. The upper floor consists of six classrooms, a conference room, nine offices, and four research laboratories, maintaining the same staircase and elevator configuration as the lower levels. Overall, the building comprises 22 classrooms, 36 faculty offices, laboratories, studios, restrooms, utility rooms, and shared spaces, designed to support academic and research activities. It is constructed in compliance with ASHRAE standards, ensuring high energy efficiency and optimal indoor environmental quality. The design incorporates thermal insulation, energy-efficient windows.

The thermal properties of the walls, roof, and floors are detailed in Table 1. The WWR of 30.69% is optimized to balance daylight utilization and energy efficiency, ensuring compliance with sustainability standards and occupant comfort.

Table 3. Thermal Characteristics of the Building Envelope.

Construction	U Value (W/m ² ·K)
Typical IEAD Roof - Highly Reflective R-25.64	0.23
Typical Insulated Steel Framed Exterior Wall R-12.99	0.47
Typical Insulated Exterior Mass Floor R-13.51	0.42

This study evaluates the system's performance in three Tunisian cities with distinct climatic conditions: Gabes (33.8815° N, 10.0982° E), Beja (36.7301° N, 9.1847° E), and Borma (32.7986° N, 10.3904° E). Gabes, located near the southern coast, experiences a desert climate characterized by high temperatures and low annual precipitation. Beja has a Mediterranean climate, marked by cold, rainy winters and hot, dry summers. Borma, situated in the southern desert, endures an

extremely arid climate with high temperatures and significant diurnal temperature variations. The figure 4 illustrates the climatic classifications within Tunisia.

Meteorological data were obtained from the OneBuilding database [54], which provides EnergyPlus-compatible Typical Meteorological Year (TMY) files derived from historical measurements and satellite data., and annual simulations of the building’s electricity, heating, cooling, and hot water demands were conducted for each location using EnergyPlus. The Köppen-Geiger climate classification as shown in Figure 5 aligns with these climatic categorizations, ensuring consistency between the simulation inputs and the actual climatic conditions of the studied regions [55]. This will also be confirmed through the energy demand results, the level of grid independence, and their alignment with the prevailing climatic conditions. Figure 6 presents some of the schedules used in modeling the college building.

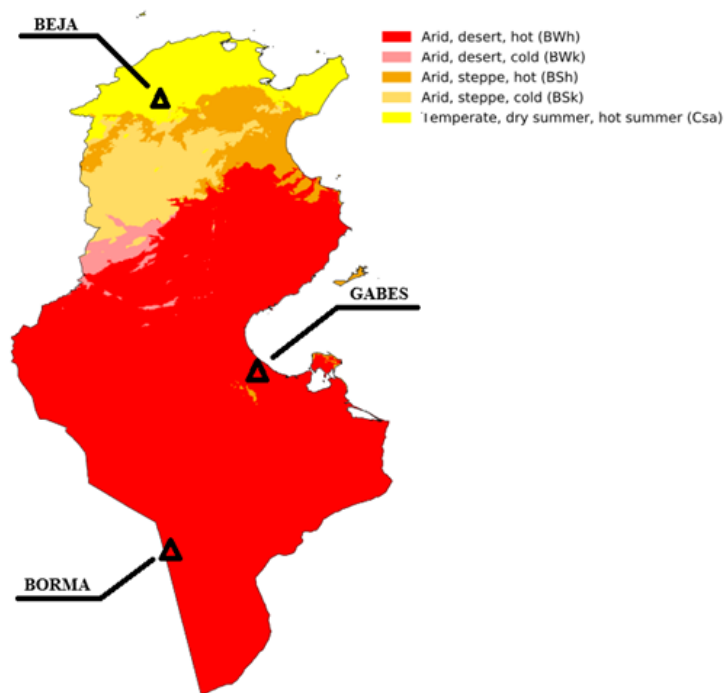
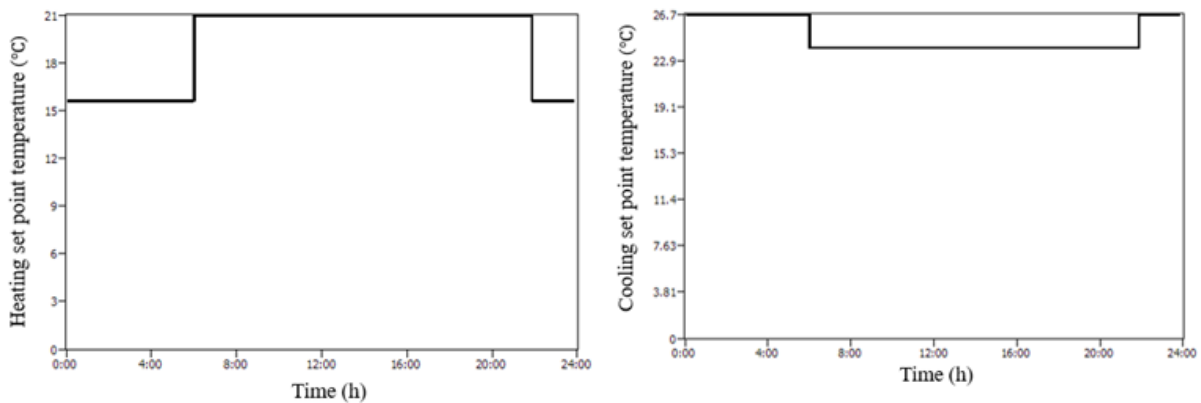


Figure 5. Köppen–Geiger Climate Zoning of Tunisia: Mapping Beja, Gabes, and Borma.



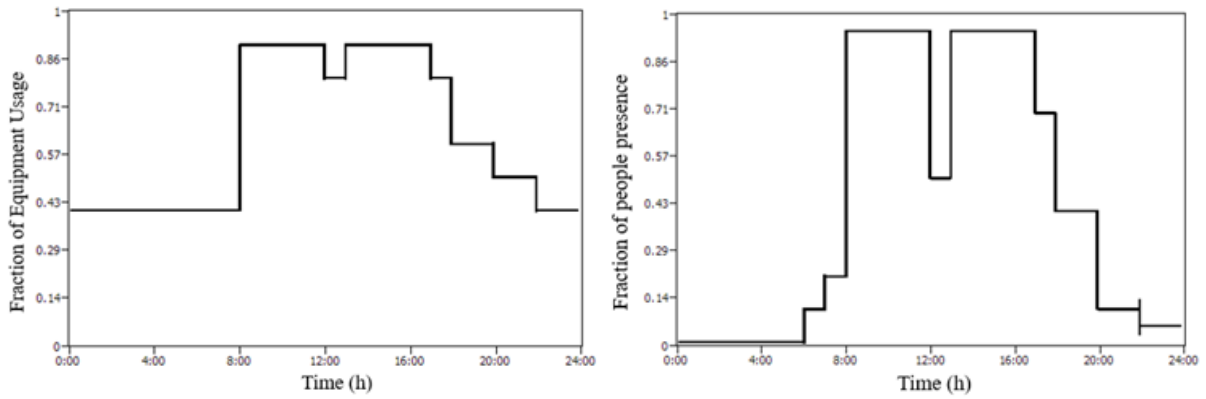


Figure 6. Some schedule diagram intended to model a large office over a 24-hour period.

5.2. Electrical Subsystem Modeling

5.2.1. PV System Setup and Modeling

To accurately simulate the performance of the photovoltaic (PV) subsystem within the hybrid energy configuration, a dual-installation strategy was adopted. PV modules were distributed between the building's rooftop and an adjacent open green area to optimize spatial utilization, reduce mutual shading, and align electricity generation with the building's hourly energy demand. Model outputs from OpenStudio were employed to ensure consistency between solar energy availability and the building's electrical load profile.

For rooftop deployment, an East–West orientation was selected to enable higher panel density and reduce tilt angle requirements while maintaining a relatively uniform energy output throughout the day. This approach has been shown to outperform conventional south-facing layouts in terms of yield per unit area, particularly in constrained urban environments [56]. Seventy percent of the rooftop area was designated for installation, and the number of modules was calculated using:

$$NPV_{roof} = \left\lfloor \frac{A_{roof, usable}}{A_{PV, proj}} \right\rfloor \quad (11)$$

where:

- NPV_{roof} : Total number of rooftop PV modules
- $A_{roof, usable}$: Usable rooftop area (70% of the total roof area)
- $A_{PV, proj}$: Projected area of a single panel (accounting for tilt)
- $mod(x, 1)$: Extracts the decimal part, ensuring the result is an integer

In the green area, a south-facing configuration was adopted to maximize solar irradiance during winter months. Inter-row spacing was determined to minimize shading based on panel geometry and solar position. The minimum required spacing was computed as [57]:

$$D_{min} = H_p \times \cos(\beta) \times \left(1 + \frac{\cos(\gamma) \times \tan(\beta)}{\tan(\alpha)} \right) \quad (12)$$

where:

- D_{min} : Minimum spacing between rows (m).
- H_p : Panel height (1.134 m).
- β : Tilt angle (34°).
- γ : Solar azimuth angle (24°).
- α : Solar altitude angle (25°).

This formulation (Eq. 12) is derived from the trigonometric relationship governing the projection of a tilted panel's shadow onto the adjacent row. The shading scenario was analyzed for the winter solstice, specifically the hour following sunrise on December 21, when the sun is at its lowest effective angle. The underlying geometric model is illustrated in Figure 7, which shows the angular relationships and shadow lengths used to derive the spacing requirement. Based on this analysis, a spacing of 2.19 m was implemented to prevent self-shading and maximize annual energy capture.

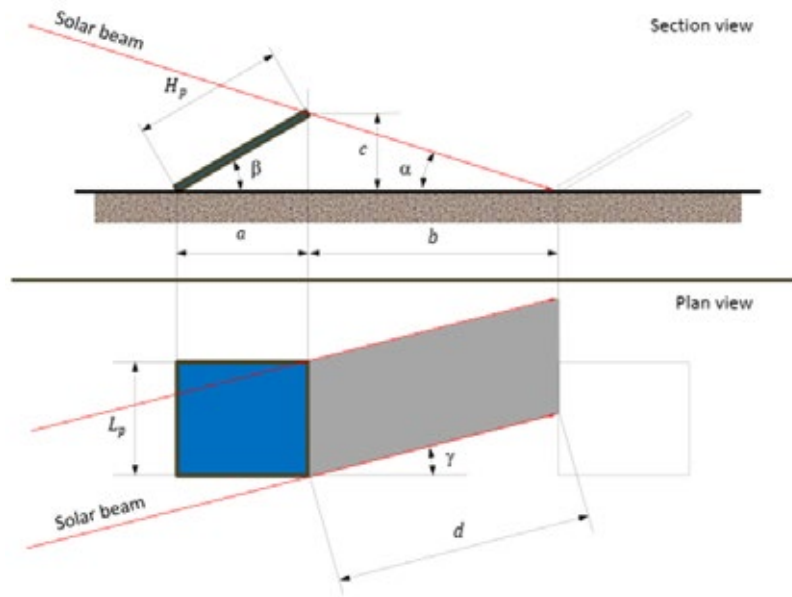


Figure 7. Shading Geometry of Tilted PV Rows (Adapted from Malara et al., 2016).

To compute the real-time output of the PV system, a temperature- and irradiance-dependent performance model was used [58]:

$$E_{pv} = P_{STC} \left[1 + \beta_p (T_{cell} - T_{STC}) \right] \frac{H_t}{H_{STC}} \quad (13)$$

where:

- E_{PV} : Actual power output (W).
- P_{STC} : Rated power under standard test conditions (STC).
- β_p : Power temperature coefficient (%/°C).
- T_{cell} : PV cell temperature (°C).
- T_{STC} : Standard temperature (25°C).
- H_t : Real-time global irradiance (W/m²).
- H_{STC} : Reference irradiance at STC (1000 W/m²).

The PV cell temperature was estimated using an empirical linear correlation [59]:

$$T_{cell} = T_{\infty} + 7.8 \times 10^{-2} H_t \quad (14)$$

where:

- T_{∞} : Ambient air temperature (°C)
- H_t : Incident solar irradiance (W/m²)

To reflect realistic deployment in such climates, a high-efficiency N-Type TOPCon bifacial PV module was selected. Rated at 450 W, this technology offers enhanced thermal stability, lower degradation rates, and bifacial gains. These characteristics make it well-suited for semi-arid

conditions with high irradiance and temperature fluctuations. The main specifications of the module are listed in Table 4.

This choice is further validated by findings from the Atlas of PV Solar Systems across Libyan Territory, which emphasizes the strong thermal resilience and bifacial performance advantages of N-Type modules in desert and semi-desert environments [60].

Following this engineering approach, the final system layout comprised 470 rooftop panels and 667 ground-mounted panels. This configuration maximizes spatial utilization, reduces mutual shading losses, and ensures a coherent match between solar energy production and the building's electrical demand.

Table 4. Electrical and physical characteristics of the selected PV module [61].

Parameter	Value	Unit
Type	103b	-
Module short-circuit current at reference conditions	14.45	A
Module open-circuit voltage at reference conditions	38.51	V
Module voltage at max power point and reference conditions	33.11	V
Module current at max power point and reference conditions	13.58	A
Rated Power (Pmax)	450 W	-
Efficiency	22.5%	-
Cell Type	N-Type TOPCon, bifacial	-
Number of Cells	108 half-cut monocrystalline	-
Dimensions	1762 × 1134 × 30 mm	mm
Operating Temperature Range	-40 °C to +85 °C	°C
Nominal Operating Cell Temp	43 °C ± 2 °C	°C
Power Temperature Coefficient	-0.30 %/°C	%/°C
Weight	Approx. 24.9 kg	kg
Mechanical Protection	Double-glass, hail-resistant	-

5.2.2. Battery Storage System

To support electrical autonomy and ensure continuity of supply during periods of low solar production, a modular lithium-iron phosphate (LiFePO₄) battery system was integrated into the hybrid energy configuration. Designed for long-term stationary applications in institutional buildings, the system provides enhanced reliability, operational safety, and capacity scalability. The battery and inverter components were modeled using Types 47 and 48 in TRNSYS, with key operational parameters—such as round-trip efficiency, inverter losses, and self-discharge rate defined according to manufacturer data. The dynamic behavior of the battery was governed by the following energy balance equation, implemented within the system's control strategy [62]:

$$SoC(t) = SoC(t-1) \cdot (1 - \sigma) + \left(P_{PV}(t) - \frac{P_L(t)}{\eta_{inv}} \right) \times \eta_b \quad (15)$$

where:

- $SoC(t)$: Battery state of charge at time t.
- σ : Daily self-discharge rate.
- $P_{PV}(t)$: Power generated by the photovoltaic system (W).
- $P_L(t)$: Electrical load demand at time t (W).
- η_{inv} : Inverter efficiency.
- η_b : Battery charge/discharge efficiency.

This formulation ensures accurate real-time tracking of energy flow between the PV generation, load demand, and storage system, while accounting for conversion losses and realistic charge-discharge behavior under varying operating conditions.

Table 5. Battery Technical Specifications [63].

Parameter	Value
Type	Type 47
Battery Chemistry	LiFePO ₄ (Lithium-Iron Phosphate)
Usable Energy Capacity (per unit)	13.44 kWh
Cycle Life @ 80% DoD	>5000 cycles
Charging Efficiency	95%
Inverter Efficiency	90%
Daily Self-Discharge Rate	1%
Thermal & Electrical Protection	Integrated

5.3. Geothermal Borehole Design and Simulation

The geothermal heat exchanger system in this study is modeled as a vertical closed-loop field consisting of multiple boreholes, each 150 m in depth. To evaluate thermal performance and long-term ground interaction, the system was simulated using TRNSYS, integrating both thermal load variations and field geometry effects. The methodology includes two main components: (1) a robust numerical framework for ground temperature prediction, and (2) a parametric evaluation of various borehole field configurations across the selected Tunisian cities.

5.3.1. Ground Temperature Modeling in TRNSYS

To simulate the long-term thermal behavior of the borehole heat exchanger field, the Duct Storage Model (DST) implemented in TRNSYS (Type 557) is employed. Rather than solving the full transient 3D field $T(r, z, t)$, the model uses a semi-analytical approach based on precomputed g -functions to capture the ground's temperature response to a unit thermal pulse. This method accounts for borehole depth, radius, spacing, and soil thermal properties. The borehole wall temperature is estimated as [64]:

$$T_b(t) = T_0 - \frac{\dot{q}}{2\pi\lambda_s} \cdot g\left(\frac{t}{t_s}, \frac{r_b}{H}, \frac{B}{H}\right) \quad (16)$$

where $T_b(t)$ is the borehole wall temperature, T_0 is the undisturbed ground temperature, \dot{q} is the unit heat injection rate, λ_s is the soil thermal conductivity, r_b is the borehole radius, B is the spacing between boreholes, and H is the borehole depth. The characteristic time t_s is defined as $\frac{H^2}{9\alpha}$, where α is the ground thermal diffusivity.

To account for the cumulative effect of previous thermal loads, TRNSYS applies a Multiple Load Aggregation Algorithm (MLAA). The fluid temperature in the borehole loop is then approximated by [65]:

$$T_f,t = T_0 - \left(\frac{q_t R_b}{H}\right) - \left(\frac{1}{\lambda H}\right)(MLAA) + T_p,t \quad (17)$$

where T_f,t is the average fluid temperature at time t , q_t is the thermal load, R_b is the borehole resistance, and T_p,t is a temperature penalty that accounts for long-term field interaction. This methodology allows TRNSYS to capture both transient and cumulative thermal behavior of the ground with computational efficiency and has been validated in prior work.

The detailed input parameters used to characterize the borehole system are listed in Table 6.

Table 6. Specifications of the Borehole GHX.

Parameters	Value	Unit
Type	103b	-
Header Depth	1	m
Borehole Radius	0.1016	m
Number of Boreholes in Series	1	-
Number of Radial Regions	1	-
Number of Vertical Regions	10	-
Storage Thermal Conductivity	4.68	kJ/hr.m.K
Storage Heat Capacity	2016	kJ/m ³ /K
Fill Thermal Conductivity	1.3	W/m.K
Pipe Thermal Conductivity	0.46	W/m.K
Gap Thermal Conductivity	5.04	kJ/hr.m.K
Gap Thickness	0	m
Insulation Indicator	0	-
Insulation Height Fraction	0.5	-
Insulation Thickness	0.0254	m
Insulation Thermal Conductivity	1	kJ/hr.m.K
Number of Simulation Years	1	-
Maximum Storage Temperature	100	C
Initial Surface Temperature of Storage Volume	7.96	C
Initial Thermal Gradient of Storage Volume	0	any
Number of Preheating Years	0	-
Maximum Preheat Temperature	15	C
Minimum Preheat Temperature	10	C
Thermal Conductivity of Layer	4.68	kJ/hr.m.K
Heat Capacity of Layer	2016	kJ/m ³ /K
Thickness of Layer	1000	m

5.3.2. Simulation of Borehole Configurations

was conducted across a wide range of configurations, combining different borehole counts (Nb = 75, 90, 110, 130, 150, 170, 175) with varying spacing distances (Sp = 4 m, 5 m, 6 m, 7 m, 8 m). This resulted in 35 unique configurations, each applied to the three case-study cities—Gabes, Beja, and Borma—to assess their thermal performance under distinct climatic and demand conditions. The simulations aimed to assess the thermal response and long-term ground temperature behavior associated with each layout, ultimately supporting the identification of thermally and spatially optimal configurations prior to multi-objective optimization.

5.4. Techno-Economic and Environmental Assessment

5.4.1. Instantaneous Operating Cost Rate

To characterize the real-time economic burden associated with each system component under a given configuration (i), the instantaneous operating cost rate ($\dot{Z}_j^{(i)}$) is introduced. This metric expresses the cost of operating component j in USD per second, based on its configuration-

dependent capital cost $Z_j^{(i)}$, maintenance factor (φ), fixed annual operating hours (N_j), and component-specific service lifetime (n_j). The capital recovery factor (CRF_j) is used to annualize the investment cost over time using a constant discount rate (r), typically ranging between 10% and 15% for renewable energy projects in Africa [66], and is given by [67]:

$$CRF_j = \frac{r \times (1+r)^{n_j}}{(1+r)^{n_j} - 1} \tag{18}$$

The instantaneous cost rate for component j in configuration i is then calculated as:

$$\dot{Z}_j^{(i)} = \frac{Z_j^{(i)} \times \varphi \times CRF_j}{N_j \times 3600} \tag{19}$$

Where:

- $\dot{Z}_j^{(i)}$: instantaneous operating cost rate of component j in configuration i (USD/s).
- $Z_j^{(i)}$: capital cost of component j in configuration i (USD).
- φ : maintenance factor (1,06).
- N_j : fixed annual operating hours for component j (hours/year).
- r : discount rate (12%).
- n_j : lifetime of component j (years).

To determine the total instantaneous cost rate for a given configuration (i), the individual cost rates of all active components are aggregated:

$$\dot{Z}_{total}^{(i)} = \sum_{j=1}^m \dot{Z}_j^{(i)} \tag{20}$$

where m denotes the number of components in the system. This approach enables consistent and equitable comparison of short-term economic performance across design alternatives.

Table 7. Economic Input Parameters, Purchase Costs, and Calculation References [67].

Component	Purchase Cost Function (\$)	Operation Years
Solar Panel ¹	$Z_{PV} = 135 \times N_{PV}$	30 years
Battery ²	$Z_{Battery} = 4598.2 \times N_{Battery}$	25 years
Heater ³	$Z_{Heater} = 325 \times P_{Heater}^{0.75} \times 0.91$	10 years
Pump ⁴	$Z_p = 705.48 \times P_p^{0.71} \times \left(1 + \frac{2}{1 - \eta_p}\right)$	20 years
Heat Pump ⁵	$Z_{HP} = 20500 \times N_{HPmax}$	20 years
Pipe ⁶	$Z_{Pipe} = 1.64 \times L_{pipe}$	25 years
Borehole ⁷	$Z_{Borehole} = 7500 \times N_{Borehole}$	30 years
Collector ⁸	$Z_{coll} = 1885.79 \times N_{Coll}$	25 years

5.4.2. Levelized Cost of Energy (LCOE)

The Levelized Cost of Energy (LCOE) is a widely adopted metric for assessing the economic performance of renewable energy systems over their lifetime. It represents the average cost per kilowatt-hour (kWh) of electricity, incorporating both capital expenditures and recurrent operating costs, while accounting for financial savings due to avoided grid electricity purchases [68]. In photovoltaic-battery systems, the LCOE provides critical insight into the cost-effectiveness of different design configurations under specific regulatory and operational constraints. Given Tunisia’s restrictive legal framework, which limits surplus PV electricity sales through capped feed-in thresholds and mandates exclusive contracts with the national utility [69], two LCOE

formulations are employed:

- $LCOE_1$ is based on the total electricity generated by the PV system.
- $LCOE_2$ accounts solely for the clean electricity effectively consumed by the building, thus reflecting the economic return on actual utilization.

Both indicators are derived from a net-cost perspective, in which the financial benefit from avoiding grid electricity purchases is explicitly subtracted from the system's lifetime costs. The governing equations are:

$$LCOE_1 = \frac{Z_{electric} + NPV_{O\&M} - NPV_{savings}}{NPV_{energy}} \quad (21)$$

$$LCOE_2^{(i)} = \frac{Z_{electric} + NPV_{O\&M} - NPV_{savings}^{(i)}}{NPV_{clean\ energy}^{(i)}} \quad (22)$$

Each term in these expressions is defined and calculated as follows:

- $Z_{electric}$: the total capital investment in the PV and battery system, including modules, inverters, battery units, and associated components.
- $NPV_{O\&M}$: the net present value of operation and maintenance (O&M) costs over the project's lifetime.

Annual O&M expenses are calculated as a fixed percentage 6% of the capital cost and are discounted using a defined rate over the system lifespan:

$$NPV_{O\&M} = \sum_{t=1}^n \frac{\alpha \times Z_{electric}}{(1+r)^t} \quad (23)$$

Where α is the annual O&M rate, r is the discount rate, and n is the project duration in years.

- $NPV_{savings}$ and $NPV_{savings}^{(i)}$: the present value of financial savings accrued by avoiding the purchase of grid electricity. These are computed by multiplying the energy offset from the grid by the unit price of electricity in each year and discounting the result:

$$NPV_{savings} = \sum_{t=1}^n \frac{E_t \times p_e}{(1+r)^t} \quad (24)$$

$$NPV_{savings}^{(i)} = \sum_{t=1}^n \frac{E_{clean,t}^{(i)} \times p_e}{(1+r)^t} \quad (25)$$

where p_e is the grid electricity tariff, E_{pv} is the PV electricity produced in year t , and $E_{clean,t}^{(i)}$ is the portion consumed by the building for configuration i .

- NPV_{pv} and $NPV_{clean}^{(i)}$: the present value of renewable energy produced and consumed, respectively, over the project lifetime. These are calculated as:

$$NPV_{pv} = \sum_{t=1}^n \frac{E_{pv}}{(1+r)^t} \quad (26)$$

$$NPV_{clean}^{(i)} = \sum_{t=1}^n \frac{E_{clean,t}^{(i)}}{(1+r)^t} \quad (27)$$

By incorporating both cost flows and avoided grid electricity expenses, this dual-formulation enables a robust comparison of system configurations. $LCOE_1$ represents the theoretical minimum cost of energy production, while $LCOE_2$ provides a policy-relevant metric that captures actual self-consumption performance under restrictions on feeding surplus energy into the grid.

5.4.3. Payback Time Estimation

The Payback Time (PBTM) metric quantifies the number of years required for the cumulative

financial savings resulting from avoided grid electricity purchases to recover the total system investment [70]. It complements the LCOE framework by shifting the analysis from unit cost to return period. Two formulations are defined:

- PBTM₁, which assumes that all electricity generated by the PV system is fully utilized.
- PBTM₂, which considers only the clean electricity actually consumed by the building under configuration i.

The evaluation procedure follows three main steps:

Step 1: Compute the Total Capital Cost:

For each configuration i, the total capital cost $Z_{total}^{(i)}$ includes both the initial investment and the discounted O&M costs of all system components:

$$Z_{total}^{(i)} = Z_{inv}^{(i)} + \sum_{j=1}^m NPV_{O\&M}^{(i)} \quad (28)$$

Where:

- $Z_{inv}^{(i)}$: initial investment cost of the complete system under configuration i,

$$NPV_{O\&M,j}^{(i)} = \sum_{t=1}^{n_j} \frac{\alpha \times Z_j^{(i)}}{(1+r)^t} \quad (29)$$

- $NPV_{O\&M,j}^{(i)}$: discounted O&M cost for component j,
- α : annual O&M rate,
- r : discount rate,
- n_j : lifetime of component j,
- m : number of components.

Step 2: Calculate Annualized Energy Savings:

The present value of financial savings is converted into an equivalent annual amount using the Capital Recovery Factor (CRF):

$$CRF(r, n) = \frac{r \times (1+r)^n}{(1+r)^n - 1} \quad (30)$$

$$\bar{C}_{PV}^{(i)} = \left(\sum_{t=1}^n \frac{E_{PV,t}^{(i)} \times p_e}{(1+r)^t} \right) \times CRF(r, n) \quad (31)$$

$$\bar{C}_{clean}^{(i)} = \left(\sum_{t=1}^n \frac{E_{clean,t}^{(i)} \times p_e}{(1+r)^t} \right) \times CRF(r, n) \quad (32)$$

Where:

- $\bar{C}_{PV}^{(i)}$: annualized savings based on total PV generation,
- $\bar{C}_{clean}^{(i)}$: annualized savings based on clean electricity consumed,
- $E_{PV,t}^{(i)}$: total photovoltaic energy produced in year t under configuration i,
- $E_{clean,t}^{(i)}$: clean electricity actually consumed in year t under configuration i,
- p_e : grid electricity price,
- r : discount rate,
- n : evaluation period (years).

Step 3: Compute Payback Times [70]:

$$PBTM_1^{(i)} = \frac{Z_{total}^{(i)}}{\bar{C}_{PV}^{(i)}} \quad (33)$$

$$PBTM_2^{(i)} = \frac{Z_{total}^{(i)}}{\bar{C}_{clean}^{(i)}} \quad (34)$$

While PBTM₁ reflects an optimistic return period under ideal utilization, PBTM₂ offers a more conservative and policy-aligned estimate based on actual self-consumption. Together, they provide a balanced perspective on the economic viability of each configuration.

5.4.4. Environmental Damage Cost

To complement the techno-economic evaluation, this study quantifies the environmental damage cost resulting from carbon dioxide (CO₂) emissions associated with grid electricity consumption. This cost represents a direct monetary penalty linked to fossil-based power generation and is computed using the following expression [71]:

$$C_{CO_2} = EF_{CO_2} \times E_t \times \varphi_{CO_2} \quad (35)$$

Where:

C_{CO_2} : total environmental damage cost (USD/year).

EF_{CO_2} : emission factor of grid electricity (kg CO₂/kWh).

E_t : annual electricity consumption from the grid (kWh/year).

φ_{CO_2} : social cost of carbon, assumed to be 70 USD/ton CO₂ [72].

Following the methodology outlined in [71], this study adopts an emission factor of 0.658 kg CO₂/kWh, derived from a recent life-cycle assessment of gas-based power plants in Iran [73]. While the referenced context pertains to Iran, where natural gas is also the primary fuel, the emission factor remains applicable to Tunisia's case, whose electricity sector similarly relies almost entirely on gas, in contrast with oil-dominant neighboring systems such as Libya [74].

5.5. Multi-Criteria Configuration Ranking

To ensure a balanced and sustainable hybrid renewable energy system design, a multi-criteria optimization approach over a discrete configuration space was adopted. This approach relied on the evaluation of 35 predefined configurations per city, generated through TRNSYS simulations by varying the number of geothermal boreholes (Nb) and their spacing (Sp). The assessment focused on four key indicators: required borehole volume, long-term thermal accumulation in the soil, instantaneous operating cost rate, and the contribution of grid electricity to annual consumption. Based on the Weighted Sum Model (WSM), the normalized indicators were aggregated into a single objective function to rank system configurations according to their composite performance, in line with established methodologies in the sustainability assessment literature [75].

5.5.1. Performance Scoring Methodology

• Evaluation Indicators:

Each configuration X is evaluated based on the following four key indicators:

- V(X): Ground volume required for borehole deployment (m³).
- ΔT(X): Long-term soil thermal accumulation (°C).
- Ż(X): Instantaneous cost rate (USD/s).
- G(X): Grid electricity contribution to annual consumption (MWh).

Configurations exceeding the critical thermal threshold of ΔT(X) ≥ 4°C were excluded to ensure long-term ground stability.

• Normalization:

To ensure fair comparison among indicators with different units and scales, normalization was applied using the following formula for all indicators to be minimized:

$$f_i^{norm}(X) = \frac{f_i^{max} - f_i(X)}{f_i^{max} - f_i^{min}} \quad (36)$$

This applies to: V(X), ΔT(X), Ż(X), and G(X).

• **Composite Objective Function:**

A weighted sum model was used to combine the normalized indicators into a single objective function $F(X)$:

$$F(X) = \omega_{\Delta T} \cdot f_{\Delta T}^{norm}(X) + \omega_V \cdot f_V^{norm}(X) + \omega_{\dot{Z}} \cdot f_{\dot{Z}}^{norm}(X) + \omega_G \cdot f_G^{norm}(X) \quad (37)$$

The weights reflect the relative importance of each indicator and are summarized as follows:

Table 8. Optimization Indicators and Weights.

Indicator	Symbol	Objective	Weight (ω)
Soil Accumulation	ΔT	Minimize	0.50
Ground Volume	V	Minimize	0.25
Instantaneous Cost Rate	\dot{Z}	Minimize	0.15
Grid Contribution	G	Minimize	0.10

• **Ranking Algorithm**

The following evaluation steps were performed:

1. Filter out all configurations violating the thermal stability condition $\Delta T(X) \geq 4^\circ\text{C}$.
2. Determine the minimum and maximum values for each indicator across the remaining configurations.
3. Normalize all indicators using the above formula.
4. Compute the composite score $F(X)$ for each configuration.
5. Rank configurations in descending order of $F(X)$; the top-ranked configuration is selected as optimal.

5.5.2. Analytical Significance

This optimization framework integrates thermal, economic, and spatial considerations into a unified decision-making process. It prioritizes thermal stability (through the dominant weight assigned to ΔT) while ensuring that ground area usage, operational cost, and dependence on grid electricity remain within acceptable limits. The methodology allows policy-makers and designers to identify system configurations that are technically viable, economically feasible, and environmentally appropriate under local constraints.

5.6. Assumptions, Limitations, and Uncertainties

The proposed methodology is grounded in simulation-based evaluation, yet several assumptions and uncertainties influence the precision and transferability of the results:

- **Model Validation:** No field data were available to calibrate or validate the models; this limitation is acknowledged, and future work will focus on field-based measurements to refine key parameters and improve result reliability.
- **Assumptions:** Ground thermal properties are considered homogeneous; system components operate under ideal control logic with no degradation or faults over the 30-year lifespan.
- **Limitations:** The TRNSYS DST model captures long-term borefield dynamics using precomputed g-functions, omitting short-term transients and subsurface heterogeneity. Dynamic weather data is drawn from Typical Meteorological Year (TMY) files, which may not reflect extreme climatic variability. The additional pipe lengths required for wider borehole spacing are not modeled, potentially underestimating pressure drops, auxiliary pump energy, and associated thermal losses. The omission of battery degradation may further limit the assessment of long-term system viability.
- **Uncertainties:** Total PV yield uncertainty is $\sim 9.1\%$, driven by transposition modeling (6%), irradiance inputs, and module temperature estimation (3.5%). Economic variability is also

significant—PV module prices, for instance, range between \$980/kW and \$4510/kW, indicating a ±130% fluctuation margin.

These factors are in line with established modeling practices for hybrid renewable energy systems and reflect a growing consensus in the literature on the need for methodological transparency when accounting for real-world operational variability [76].

6. RESULTS AND DISCUSSION

This section begins by presenting the results of the reference configuration, which consists of a system with 75 geothermal boreholes spaced 4 meters apart.

This configuration was selected as a suitable starting point for evaluating the system’s performance under the assumed climatic conditions, spatial constraints, and the building’s specific energy demand.

The results of this configuration revealed several critical challenges, most notably a high level of thermal accumulation in the ground ($\Delta T = 9.9^\circ\text{C}$), substantial reliance on electricity from the grid (32.65%), and a significant environmental cost associated with this dependence.

Based on these findings, a multi-objective optimization approach was adopted to identify the optimal configurations in terms of thermal performance, economic feasibility, and environmental sustainability.

Each configuration was evaluated using four primary indicators: ground thermal accumulation, total borefield volume, instantaneous cost rate (\dot{Z}), and the level of dependency on the national electricity grid. In addition to these indicators, payback time (PBTM) and levelized cost of energy (LCOE) were incorporated as supplementary metrics to reflect the economic viability of each configuration, enabling a comprehensive comparison that accounts for the technical, environmental, and financial dimensions of the energy system under study. Simulation results are shown in Table 9.

These results correspond to the reference configuration, which served as the baseline for evaluating and comparing the subsequent system configurations.

Table 9. summarizes climate-based energy demand, guiding the optimization.

City	Climate Type	Annual Energy Demand (MWh)	Remarks
Borma	Hot arid	1052.51	Highest demand due to harsh climatic conditions
Gabes	Hot semi-arid	996.59	Moderately high demand
Beja	Mild Mediterranean	977.86	Lowest demand due to temperate climate

Figure 8a and 8b illustrate the hourly distribution of electricity and hot water demand for the reference configuration.

The plots reveal a recurring daily pattern of higher daytime consumption and lower night-time demand, with seasonal fluctuations reflecting climatic and operational differences across the three cities.

The hot water demand was assumed identical across locations, allowing the analysis to focus on how electric heater consumption impacts the total load in each climate.

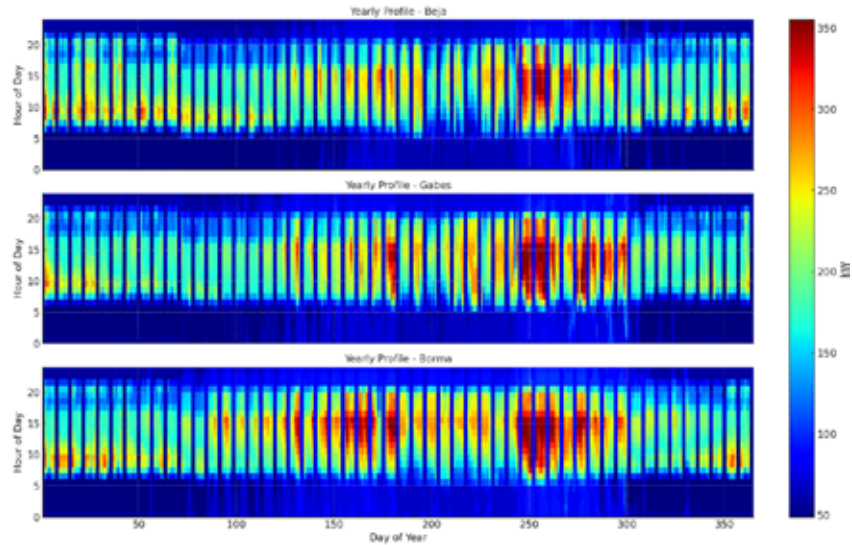


Figure 8a. Hourly Power Demand Across the Year – Beja, Gabes, and Borma.

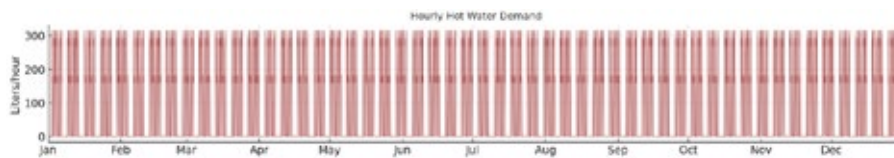


Figure 8b. Hourly Hot Water Demand – Common Profile for All Cities.

Figure 9 shows the annual electricity consumption breakdown by load type for the reference configuration. Lighting and electrical equipment represent the largest share, followed by heating and cooling systems, while the contribution of circulation pumps remains limited. Heat pump consumption is highest in Borma and lowest in Beja, while Beja also records relatively high electric heater usage due to reduced solar radiation during frequent cloudy periods.

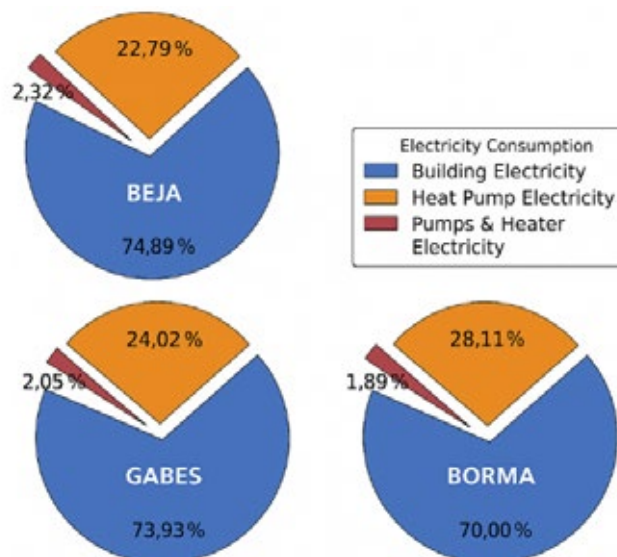


Figure 9. Annual Electricity Use by Load Type per City – Reference Configuration.

Figure 10 illustrates the hourly distribution of annual heating and cooling loads across the three cities. The results reveal a clear dominance of cooling demand, particularly from May to October, while heating needs remain limited in both duration and intensity. The peak cooling loads reached approximately 1175 kW in Beja, 1051 kW in Gabes, and 870 kW in Borma, whereas

peak heating loads ranged between 324 kW and 416 kW. It should be noted that these loads represent the ideal case where no upper limit is set on the number of active heat pump units. As mentioned in the methodology section, the system was constrained to a maximum of 16 units, intentionally leaving rare peak demands unmet to reduce investment costs. Nevertheless, these theoretical loads reveal the underlying thermal imbalance between heating and cooling a pattern that persists even under the 16-unit constraint, highlighting the climatic characteristics of the studied regions. This persistent thermal imbalance stands as the primary driver of ground heat accumulation, the severity of which varies across configurations depending on the number and spacing of boreholes.

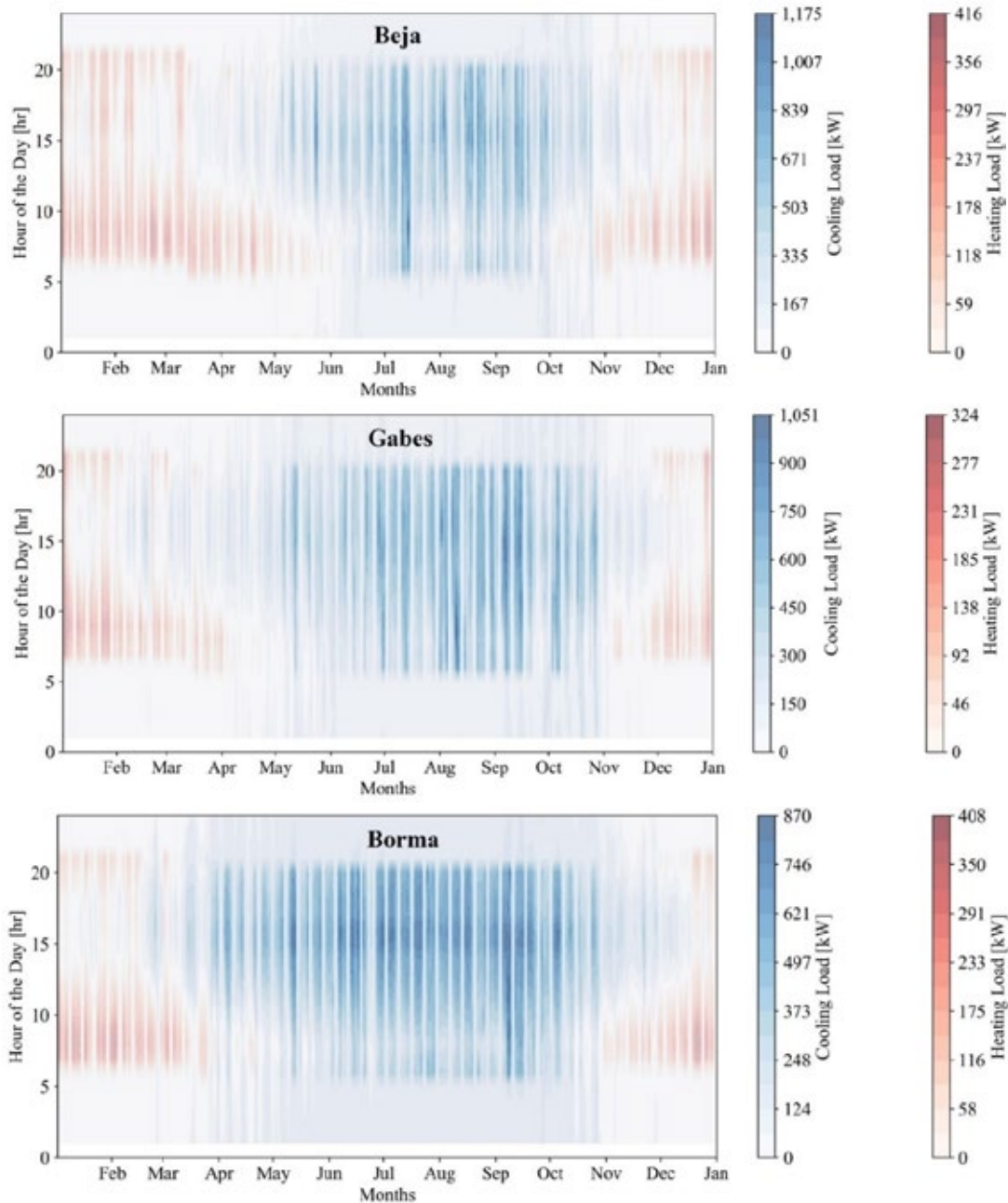


Figure 10. Annual Hourly Heating and Cooling Load Profiles – Beja, Gabes, and Borma.

The annual simulation of battery performance, as illustrated in Figure 12, reveals a clear contrast between winter and summer in terms of charging and discharging behavior. In July, high solar radiation levels, as shown in Figure 11, enabled daily average states of charge to exceed 50% across

all locations, allowing the battery system to reliably cover nighttime demand. In contrast, January exhibited significantly lower radiation, with the average state of charge dropping to around 17%, leading to rapid battery depletion and increased reliance on the electrical grid.

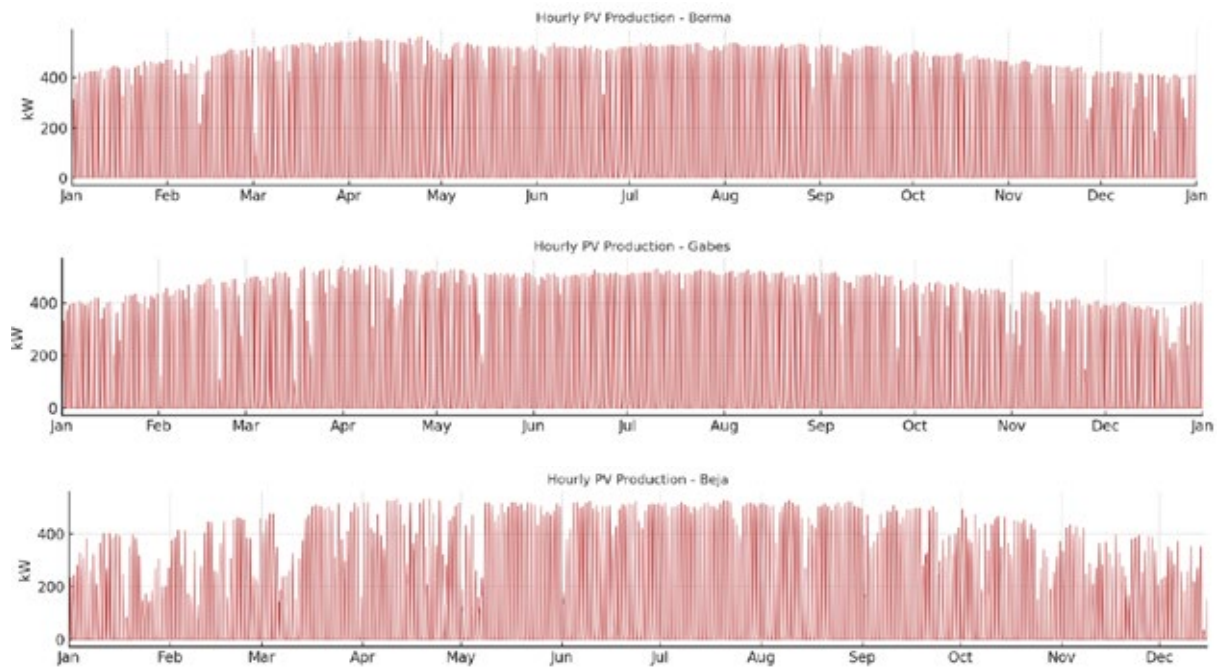


Figure 11. Hourly Photovoltaic Power Generation over the Year – Beja, Gabes, and Borma.

While the proposed optimization primarily addresses the issue of thermal imbalance caused by dominant cooling loads, it also contributes positively to reducing grid dependency, as will be discussed later. Nonetheless, the results highlight the need to explore complementary solutions, such as integrating additional energy sources alongside PV, to mitigate the winter shortfall .

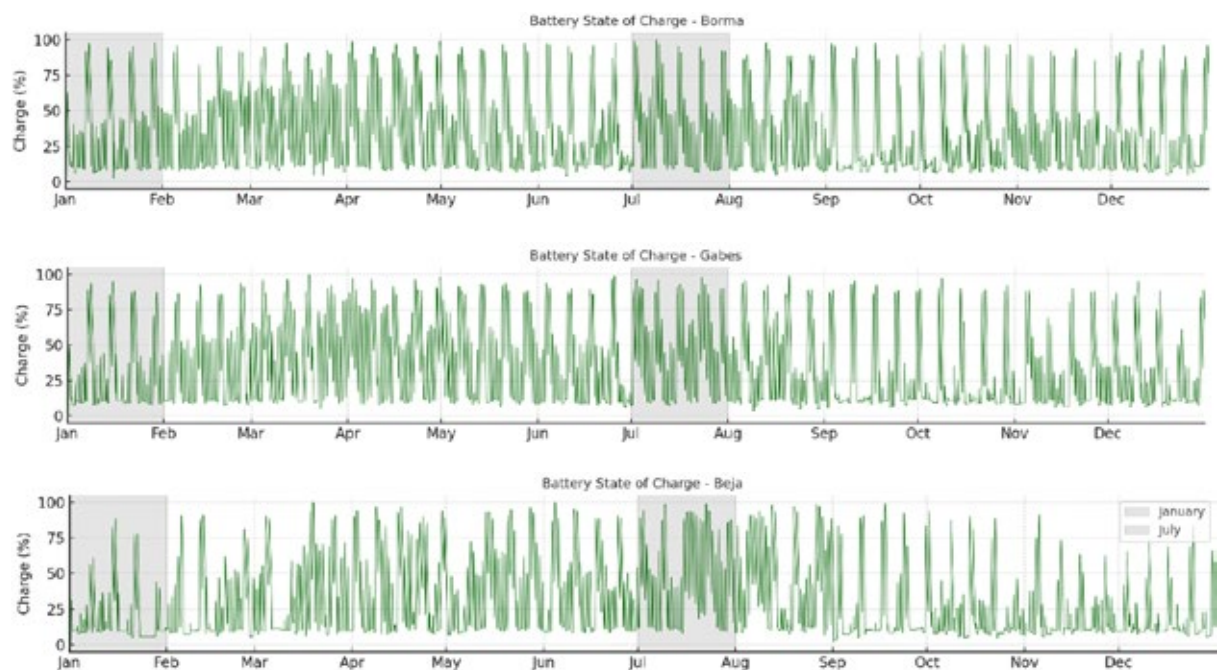


Figure 12. Battery State of Charge Over the Year – Beja, Gabes, and Borma.

The simulation results for the reference configuration, which assumes a limited surface area for ground heat exchanger installation—with boreholes installed beneath part of the area designated for photovoltaic panels to optimize land use—revealed a progressive pattern of thermal accumulation in the soil due to the close spacing of boreholes. This buildup is reflected in the gradual rise in both the ground temperature and the temperature of the fluid returning to the geothermal heat pump, as illustrated in Figure 13. Such thermal imbalance increases operational stress on the heat pump, reduces its coefficient of performance (COP) by up to 20%, with variations observed across the three cities following the same imbalance-driven pattern, and raises energy consumption, potentially leading to early system failure during the initial years of operation. This challenge is particularly relevant in cooling-dominated climates, such as Tunisian cities. The scenario underscores the limitations of the 75/4 borefield configuration in achieving long-term thermal balance, thereby highlighting the need to explore alternative borefield layouts that ensure more stable performance while addressing sustainability goals and spatial constraints—topics addressed in the following sections.

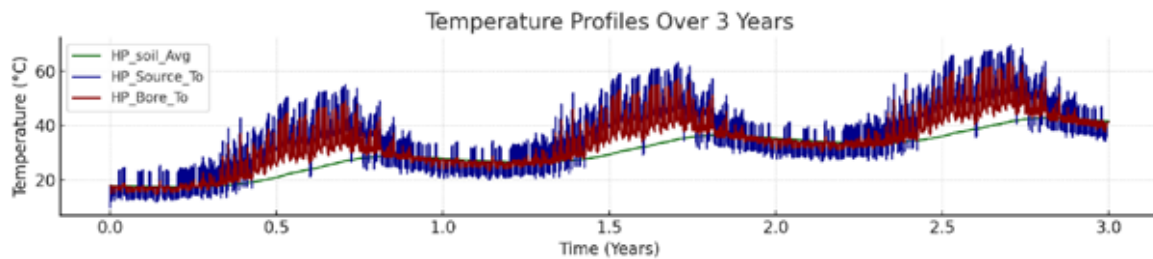


Figure 13. Evolution of Soil and Fluid Temperatures Over Three Years in Beja – Reference Configuration.

Simulation results show that the energy system, under the adopted reference configuration, remains partially dependent on the electrical grid, with the extent of reliance varying by location and season. In Beja, grid electricity covers 32.65% of the annual energy demand, compared to 26.67% in Gabes and 27.34% in Borma, reflecting regional differences in solar contribution, as illustrated in Figure 14.

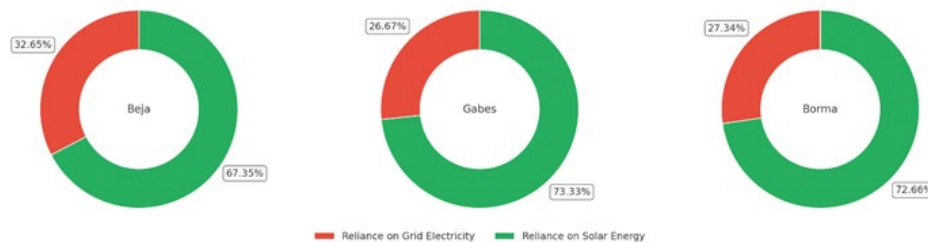


Figure 14. Distribution of Annual Electricity Supply between Grid and Renewable Sources under the Reference Geothermal Configuration (Nb = 75, Sp = 4 m).

This dependency is primarily attributed to the system’s design parameters, particularly the limited battery capacity, which is sized for only one day of autonomy and may be fully discharged during extended periods of low solar radiation. Additionally, the restricted number of PV panels is insufficient to meet total demand on cloudy days unless a significantly larger array is installed. While the thermal configuration (75 boreholes spaced at 4 meters) does lead to increased power consumption by the geothermal heat pump during summer, due to thermal accumulation and reduced cooling efficiency, its impact on overall grid reliance remains secondary compared to the PV-battery design constraints. In fact, during winter, the elevated ground temperature can enhance heat pump efficiency during heating, partially offsetting energy use. Nevertheless, the persistent imbalance between cooling and heating loads, as shown in Figure 15, remains a

structural challenge that requires rethinking the ground exchanger layout within more balanced configurations.

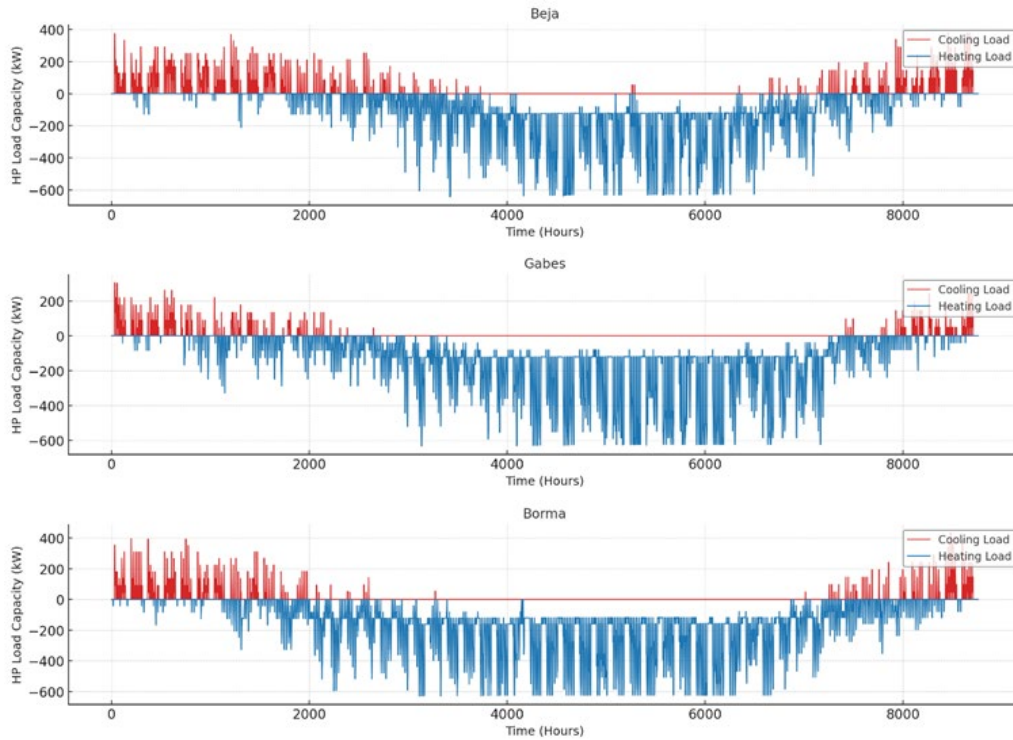


Figure 15. Heat Pump Load Variation across Tunisian Cities – Reference Configuration.

The instantaneous cost rate (\dot{Z}) serves as a dynamic indicator for evaluating the economic burden associated with each system component throughout its operational lifetime. In the adopted reference configuration, which includes 75 boreholes, the total system cost rate is approximately 7.0×10^{-3} \$/s across all three cities, owing to the identical component setup. As shown in Figure 16, batteries account for the largest share of system cost (around 36%), followed by the borehole field (approximately 34%) and the geothermal heat pump (about 19%). The remaining components, including PV panels, solar collectors, piping, and circulation pumps, collectively represent less than 10% of the total \dot{Z} .

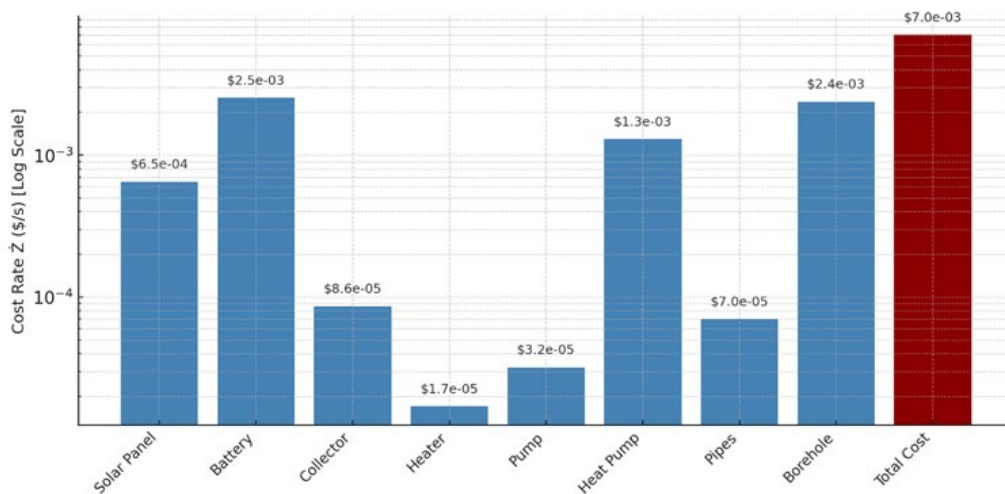


Figure 16. Component-Wise Cost Rate Distribution – Reference Configuration (Log Scale).

The following results correspond to the adopted reference configuration and are presented to establish a baseline for comparison. While some economic metrics may appear more favorable at this stage, they come at the cost of thermal performance. From an economic standpoint, two distinct formulations of the LCOE were considered, to reflect different policy scenarios. LCOE₁ assumes full utilization of PV generation (i.e., surplus energy is sold to the grid), while LCOE₂ reflects a more conservative approach aligned with the current regulatory context, where selling surplus energy to the national grid is restricted or capped. Under these assumptions, LCOE₂ ranges from 0.113 \$/kWh in Beja to 0.078 \$/kWh in Borma, whereas LCOE₁ drops significantly, reaching 0.031 \$/kWh in Beja and 0.023 \$/kWh in Borma. Similarly, PBTM were calculated. PBTM₁ reflects scenarios with surplus energy sales, while PBTM₂ represents the current policy framework where self-consumption dominates. The results indicate that PBTM₂ can exceed 41 years in Beja and decrease to 34 years in Borma, while PBTM₁ remains between 23 and 25 years, highlighting the long-term economic benefits of supportive renewable energy policies. On the environmental side, the system incurs a notable damage cost due to grid electricity usage whenever solar PV and batteries are unable to meet demand. This cost ranges from \$13,800 to \$16,400 annually, depending on the city.

Building on the preceding thermal, economic, and environmental indicators, the analysis is extended through the integration of a detailed techno-economic breakdown, which presents the component-wise cost distribution across all configurations, with the total instantaneous system cost being one of the primary indicators used for ranking and comparison, as shown in figure17. This framework offers a comprehensive analytical tool to link thermal performance with economic burden, enabling a systematic transition from the reference setup toward more optimized configurations through a multi-dimensional assessment that balances cost, thermal efficiency, spatial constraints, and sustainability.

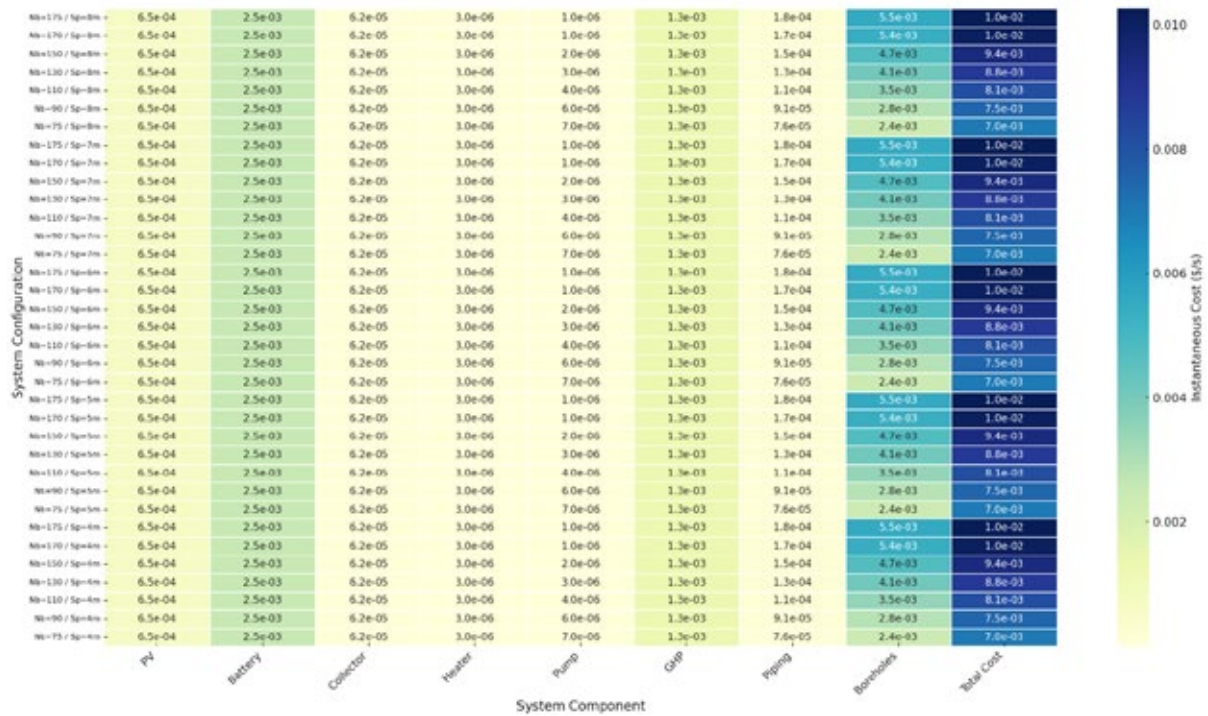


Figure 17. Instantaneous Cost Comparison across System Configurations.

Simulation results show that increasing the number of boreholes, along with improving their spatial distribution, leads to a gradual rise in the share of clean energy, increasing from 67.35% in configuration (Nb = 75 / Sp = 4 m) to 70.08% in (Nb = 175 / Sp = 8 m). This reflects a cumulative

effect of both the number and spacing of boreholes, as illustrated in Figure 18. However, the rate of improvement diminishes progressively, especially at larger spacings, indicating that the system is approaching a saturation point under the given climatic and design conditions. A similar trend in clean energy shares is observed in Gabes and Borma, where higher levels are attained due to more favorable solar conditions.

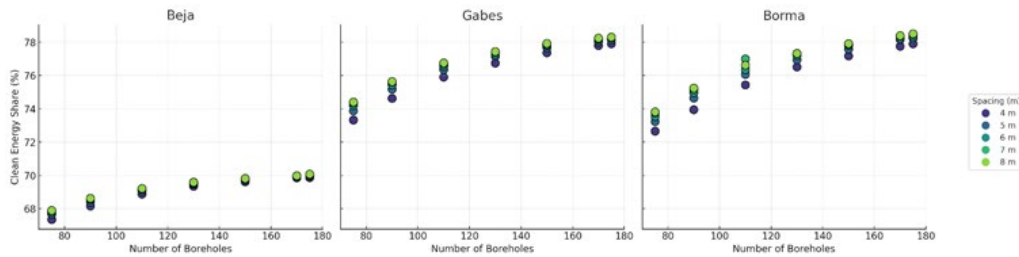


Figure 18. Clean Energy Share vs. Borefield Configuration – Three Cities.

These results highlight that a well-planned expansion of boreholes, with a carefully designed layout, contributes to enhanced energy autonomy and mitigates ground thermal accumulation. For instance, ΔT decreases from 9.9 °C in configuration (Nb = 75 / Sp = 4 m) to 1.23 °C in (Nb = 175 / Sp = 8 m), as shown in Figure 19. This decline indicates a more balanced thermal state in the ground, which is crucial for long-term system stability, as uncontrolled accumulation could lead to a gradual decline in geothermal heat pump performance. A comparable yet more pronounced accumulation is observed in Gabes and Borma, likely due to increased solar exposure.

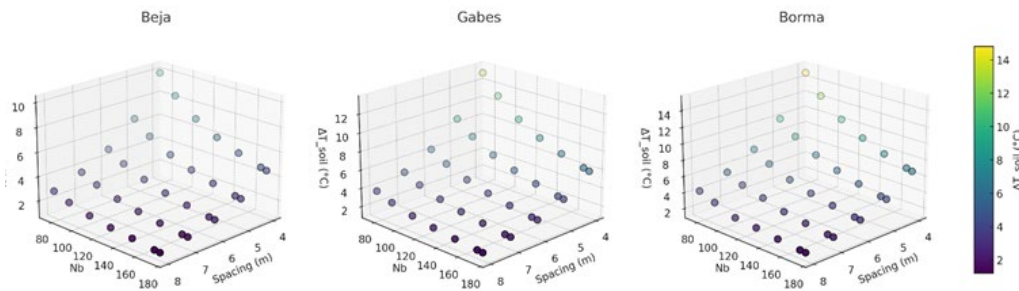


Figure 19. Soil Temperature Rise (ΔT_{soil}) vs. Borefield Configuration – Beja, Gabes, and Borma.

In parallel, the environmental damage cost associated with grid electricity emissions shows a steady decline with increased borehole numbers and spacing, as depicted in Figure 20.

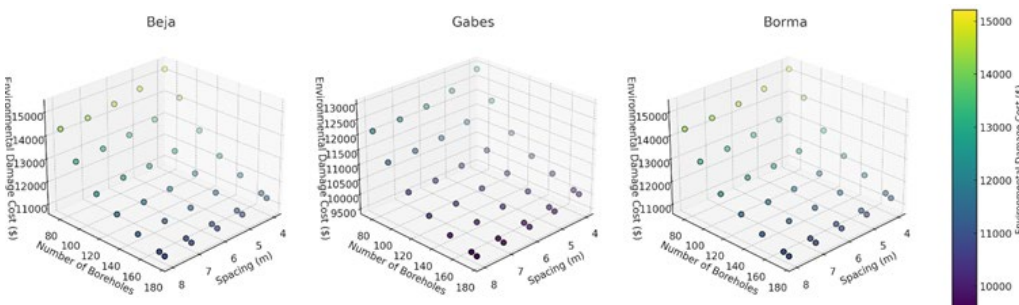


Figure 20. Environmental Damage Cost vs. Borefield Configuration – Beja, Gabes, and Borma.

At a fixed spacing of 4 meters, this cost drops from \$16,460.29 (Nb = 75) to \$14,439.35 (Nb = 175), reflecting a 12.3% reduction. When the spacing increases from 4 m to 8 m (at Nb = 175), the cost decreases slightly further to \$14,307.34—a marginal reduction of 0.9%. It is worth noting that these expansions were not initially aimed at reducing emissions, but rather at addressing

the more critical issue of ground thermal imbalance. Nonetheless, the resulting environmental benefit is significant and has been incorporated into the analysis given its relevance to the overall sustainability of the system. Comparable patterns are also noted in Gabes and Borma, shaped by their distinct climatic and demand profiles.

However, these benefits come at the expense of substantial land use, as illustrated in Figure 21. The required ground volume increases from $155,862 \text{ m}^3$ to $1,454,714 \text{ m}^3$ between the smallest and largest configurations, posing practical challenges in terms of implementation and site feasibility—particularly in urban settings or locations with strict spatial constraints.

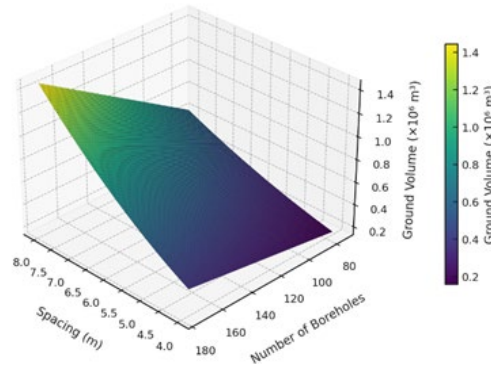


Figure 21. Required Ground Volume vs. Borehole Number and Spacing.

Despite the improvements observed at both the thermal and environmental levels, the system's instantaneous cost rate (\dot{Z}) exhibits a rising trend with the expansion of borehole configurations, reflecting the growing financial burden associated with increasing the number of boreholes. For instance, \dot{Z} increases from approximately $6.994 \times 10^{-3} \text{ \$/s}$ in configuration ($N_b = 75 / S_p = 4 \text{ m}$) to $1.025 \times 10^{-2} \text{ \$/s}$ in configuration ($N_b = 175 / S_p = 8 \text{ m}$), representing a rise of about 46.6%. This escalation is mainly attributed to the additional investment required for drilling and piping, highlighting the need for careful trade-offs between thermal and environmental performance on one hand, and economic feasibility on the other—especially in projects constrained by budget or space.

Based on the multi-criteria evaluation method, the composite objective function $F(X)$ was calculated for all configurations that satisfy the thermal stability constraint ($\Delta T_{soil} < 4^\circ\text{C}$). This function integrates four main indicators: long-term soil thermal accumulation, borefield ground volume, instantaneous operating cost rate, and annual grid electricity contribution. The weights reflect the priority of thermal sustainability (0.50), followed by ground volume (0.25), cost rate (0.15), and grid reliance (0.10). In Beja, the optimal configuration was found to be ($N_b=90 / S_p=8\text{m}$), achieving a score of $F(X) = 0.625$, reflecting a balanced trade-off between low operating cost, acceptable thermal performance, and moderate grid reliance. In Gabes, the best performance was observed for ($N_b=150 / S_p=8\text{m}$), which achieved the highest thermal stability and lowest grid contribution, but at the expense of a large ground volume ($F(X) = 0.580$). In Borma, configuration ($N_b=110 / S_p=8\text{m}$) yielded the best score ($F(X) = 0.545$), demonstrating a balance between thermal and economic indicators without a clear advantage in any specific area. Its strength lies in the absence of trade-offs, making it a stable yet moderately efficient solution. Overall, the configurations selected via $F(X)$ represent well-calibrated and promising options, though further improvements remain necessary particularly in reducing spatial requirements and integrating complementary cooling strategies to ensure long-term system stability. The characteristics of these top-performing configurations, based on their integrated thermal, technical, and economic profiles, are summarized in Table 10 and Table 11, which respectively

present the thermal-technical and techno-economic attributes of the selected solutions in each city.

Table 10. Top Configurations per City Based on F(X).

City	Configuration	F(X)	ΔT_{soil} (°C)	Ground Volume (m ³)	Grid Contribution (MWh)	Ż Cost Rate (\$/s)
Beja	Nb=90 / Sp=8m	0.625	2.36	748,138.87	310.99	0.007
Gabes	Nb=150 / Sp=8m	0.580	1.48	1,246,898.12	216.86	0.009
Borma	Nb=110 / Sp=8m	0.545	2.61	914,391.96	248.95	0.008

Table 11. LCOE and PBTM Values for Optimal Configurations.

City	Configuration	F(X)	LCOE ₁ (\$/kWh)	LCOE ₂ (\$/kWh)	PBTM ₁ (years)	PBTM ₂ (years)
Beja	Nb=90 / Sp=8m	0.625	0.03129	0.11420	26.52	44.35
Gabes	Nb=150 / Sp=8m	0.580	0.02999	0.09116	33.28	49.96
Borma	Nb=110 / Sp=8m	0.545	0.02278	0.07984	26.90	40.27

LCOE₁ and PBTM₁ are based on total PV production; LCOE₂ and PBTM₂ on actual clean energy used. The gap reflects policy barriers to surplus compensation, which delay cost recovery and hinder the energy transition.

Tunisia’s regulatory framework [77] imposes two key constraints on self-production from renewable energy:

- (1) only systems with an installed capacity below 1 MW are exempt from pre-authorization.
- (2) self-producers are allowed to sell no more than 30% of their surplus electricity to the grid, at a fixed price and exclusively to STEG.

These restrictions reduce the financial appeal of larger decentralized renewable energy systems and hinder broader market participation.

Despite these limitations, the LCOE₂ values for the selected configurations (0.0798–0.1142 \$/kWh) compare favorably with recent studies, including 0.0745 \$/kWh in Rwanda’s grid-connected PV system [15], 0.132 \$/kWh for an off-grid hybrid system in Libya [59], 0.233 \$/kWh in Gaza’s solar street lighting project [58], and 0.313 \$/kWh in a fully isolated HRES in Palestine [76]. These differences reflect variations in irradiance, system scale, storage needs, and grid accessibility.

Sensitivity to Weight Variations:

To assess the robustness of the evaluation model, a sensitivity analysis was conducted by altering the weights assigned to the four indicators using three alternative sets:

- w1: Emphasizing cost and ground volume at the expense of ΔT_{soil} .
- w2: Equal weight distribution among ΔT_{soil} , ground volume, and cost rate.
- w3: Prioritizing thermal performance ΔT_{soil} with reduced weight on ground volume.

Results showed that rankings were highly sensitive to weight adjustments. Several configurations moved up by 20–40 positions under alternative weight sets. For example, the configuration (Nb=90 / Sp=7m) in Gabes rose from rank 47 to rank 5 under w2. Similarly, in Borma, some configurations improved their thermal ranking significantly under w3.

The most sensitive configurations are summarized in Table 12.

While weight allocations are subject to policy and economic framing, core design constraints such as thermal accumulation remain technically binding, as exceeding them compromises system performance and longevity.

Table 12. Top Configurations Most Sensitive to Weight Variations.

City	Configuration	Base Rank	Rank w1	Δ Rank w1	Rank w2	Δ Rank w2	Rank w3	Δ Rank w3
Gabes	Nb=90 / Sp=7m	47	19	▲ +28	5	▲ +42	35	▲ +12
Gabes	Nb=75 / Sp=8m	44	18	▲ +26	7	▲ +37	29	▲ +15
Beja	Nb=75 / Sp=7m	43	14	▲ +29	6	▲ +37	34	▲ +9
Borma	Nb=90 / Sp=8m	42	20	▲ +22	8	▲ +34	21	▲ +21
Borma	Nb=110 / Sp=7m	55	44	▲ +11	22	▲ +33	47	▲ +8

Spatial Constraints and Complementary Solutions:

While the composite objective function effectively guided the selection of balanced configurations, the prevailing load imbalance typical of African climates consistently results in extensive ground area requirements and a gradual thermal accumulation that remains present over time. Although these effects have been partially mitigated, they underscore the need for complementary solutions such as thermal dissipation strategies or adaptive spatial design. Potential options include the integration of cooling towers or redirecting excess heat toward swimming pools in hotels or sports complexes. These strategies represent promising avenues for future research aimed at alleviating long-term ground thermal stress.

7. CONCLUSION

This study presents a methodologically grounded assessment of a solar–geothermal hybrid energy system deployed across three climatically distinct Tunisian cities—Borma, Gabes, and Beja. High-resolution dynamic simulations using OpenStudio and TRNSYS began with a reference configuration (Nb=75 / Sp=4m) to analyze thermal behavior, grid interaction, and seasonal load variation. Initial results revealed significant thermal imbalance, with peak cooling demands (660 kW) far exceeding heating needs (324–416 kW), causing soil temperature accumulation ($\Delta T = 9.9^\circ\text{C}$) and elevated grid dependency. Battery performance was highly seasonal, averaging over 50% daily charge in July versus just 17% in January, reflecting limited solar availability in winter. Optimization showed that increasing borehole number and adjusting spacing reduced ΔT to 1.23°C while increasing clean energy contribution from 67.35% to 70.08%. However, this improvement came with a 46.6% rise in instantaneous cost rate (\dot{Z}) and a 12.3% reduction in environmental damage costs associated with grid electricity use. Trade-offs between thermal relief, land usage, and economic feasibility were evident. Similar thermal imbalance patterns were observed in Gabes and Borma, primarily driven by high cooling loads. However, the abundance of solar irradiance in these regions supported a higher share of renewable energy. These findings highlight the critical role of local climate in shaping system performance, particularly the complex relationship between solar availability, energy demand, and long-term thermal stress.

Economic viability was highly sensitive to policy context:

- Under restrictive regulations (LCOE_2), cost ranged from \$0.078 to \$0.113/kWh with PBTM_2 of 34–41 years.
- Under supportive frameworks (LCOE_1), LCOE dropped to \$0.023–\$0.031/kWh and PBTM_1 to 23–25 years.

Climate-specific optimization results showed that:

- Beja (Nb=90 / Sp=8m) achieved the best overall performance ($F(X) = 0.625$),
- Gabes (Nb=150 / Sp=8m) provided the lowest ΔT and highest clean energy share ($F(X) = 0.580$),
- Borma (Nb=110 / Sp=8m) offered a balanced configuration ($F(X) = 0.545$).

To support the broader adoption of solar–geothermal hybrid energy systems, this study

recommends the following strategic policy directions:

- Expand the PROSOL program [78] to include hybrid systems, with a focus on institutional buildings and high-demand applications.
- Establish favorable financing mechanisms, such as concessional loans or performance-based grants, to reduce the high upfront costs associated with geothermal drilling.
- Implement enabling regulatory frameworks, such as net metering or feed-in tariffs, to improve system profitability and shorten the payback period.

The realism and responsiveness of the simulation environment can be further improved in future studies through the following TRNSYS-based enhancements:

- Integrate flexible demand-side management (DSM) strategies, by adjusting load schedules within TRNSYS to prioritize the operation of high-consumption equipment (e.g., heat pumps) during peak solar production hours. This reduces reliance on the grid without compromising user comfort.
- Import real-world operational data, such as actual temperature profiles or electricity consumption from existing systems, to calibrate the model and ensure alignment with local operating conditions.
- Design and implement new TRNSYS configurations, such as swimming pools connected to ground heat exchangers or other types of thermal storage systems, to explore alternative strategies for mitigating long-term soil thermal accumulation.
- Explore the integration of cooling towers into the hybrid system, as a potential solution to reduce progressive heat buildup in the ground. This option requires further analysis to assess its economic viability and potential impact on reducing grid dependency.

Altogether, this study offers a structured foundation for guiding policy, refining modeling approaches, and advancing the practical deployment of hybrid solar–geothermal systems in climate-sensitive regions.

Author Contributions: YN: conceptualization, methodology, data curation, formal analysis, visualization, writing—original draft. HD: conceptual guidance, supervision, methodological refinement, writing—review and editing.

Funding: The authors have not disclosed any funding.

Data Availability Statement: Not applicable.

Conflicts of Interest: The authors declare no known conflicts of interest.

REFERENCES

- [1] J. J. M. Guilhoto, N. Johnstone, F. Mattion, F. Papadimoulis, R. Quadrelli, and C. Webb, “Methodology for estimation of energy physical supply and use tables based on IEA’s world energy balances,” *OECD Science, Technology and Industry Working Papers*, no. 2021/13, OECD Publishing, 2021. <https://doi.org/10.1787/d3058f43-en>
- [2] International Renewable Energy Agency, *Global Renewables Outlook: Energy Transformation 2050*, Abu Dhabi, 2020. <https://www.irena.org/publications/2020/Apr/Global-Renewables-Outlook-2020>
- [3] Y. F. Nassar, H. J. El-Khozondar, M. Elnaggar, F. F. El-Batta, R. J. El-Khozondar, and S. Y. Alsadi, “Renewable energy potential in the State of Palestine: Proposals for sustainability,” *Renew. Energy Focus*, vol. 49, p. 100576, 2024. <https://doi.org/10.1016/j.ref.2024.100576>
- [4] I. Gunnarsdottir, B. Davidsdottir, E. Worrell, and S. Sigurgeirsdottir, “Review of indicators for sustainable energy development,” *Renew. Sustain. Energy Rev.*, vol. 133, p. 110294, 2020. <https://doi.org/10.1016/j.rser.2020.110294>

- [5] T. Buettner, "World population prospects – A long view," *Economie et Statistique / Economics and Statistics*, no. 520–521, pp. 9–29, 2020. <https://doi.org/10.24187/ecoStat.2020.520d.2030>
- [6] T. Yan and X. Xu, "Utilization of ground heat exchangers: A review," *Curr. Sustain./Renew. Energy Rep.*, vol. 5, no. 3, pp. 189–198, 2018. <https://doi.org/10.1007/s40518-018-0113-9>
- [7] A. Alaidroos and M. Krarti, "Optimal design of residential building envelope systems in the Kingdom of Saudi Arabia," *Energy Build.*, vol. 86, pp. 104–117, 2015. <https://doi.org/10.1016/j.enbuild.2014.09.083>
- [8] S. Ahmadi, A. H. Fakehi, A. Vakili, and M. Moeini-Aghaie, "An optimization model for the long-term energy planning based on useful energy, economic and environmental pollution reduction in residential sector: A case of Iran," *J. Build. Eng.*, vol. 30, p. 101247, 2020. <https://doi.org/10.1016/j.jobbe.2020.101247>
- [9] D. D'Agoſtino, P. Zangheri, L. Castellazzi, and D. Paci, "The use of ground source heat pump to achieve a net zero energy building," *Energies*, vol. 13, no. 13, p. 3450, 2020. <https://doi.org/10.3390/en13133450>
- [10] H. Kim and L. Junghans, "Economic feasibility of achieving net-zero emission building (NZEB) by applying solar and geothermal energy sources to heat pump systems," *J. Clean. Prod.*, vol. 416, p. 137822, 2023. <https://doi.org/10.1016/j.jclepro.2023.137822>
- [11] Y. F. Nassar, H. J. El-Khozondar, and M. A. Fakher, "The role of hybrid renewable energy systems in covering power shortages in public electricity grid: An economic, environmental and technical optimization analysis," *J. Energy Storage*, vol. 108, p. 115224, 2025. <https://doi.org/10.1016/j.est.2024.115224>
- [12] H. Al-Najjar, C. Pfeifer, R. Al Afif, and H. J. El-Khozondar, "Performance evaluation of a hybrid grid-connected photovoltaic biogas-generator power system," *Energies*, vol. 15, no. 9, p. 3151, 2022. <https://doi.org/10.3390/en15093151>
- [13] H. Al-Najjar, H. J. El-Khozondar, C. Pfeifer, and R. Al Afif, "Hybrid grid-tie electrification analysis of bio-shared renewable energy systems for domestic application," *Sustain. Cities Soc.*, vol. 77, p. 103538, 2022. <https://doi.org/10.1016/j.scs.2021.103538>
- [14] Y. F. Nassar, H. J. El-Khozondar, M. Elnaggar, F. F. El-Batta, R. J. El-Khozondar, and S. Y. Alsadi, "Renewable energy potential in the State of Palestine: Proposals for sustainability," *Renew. Energy Focus*, vol. 49, p. 100576, 2024. <https://doi.org/10.1016/j.ref.2024.100576>
- [15] E. Hakizimana, H. Umuhoza, E. Manishimwe, and V. Kayibanda, "Economic optimization of grid-connected photovoltaic solar systems in industrial energy: Case study SULFO Ltd – Rwanda," *J. Sol. Energy Sustain. Dev.*, vol. 13, no. 2, pp. 204–229, Aug. 2024.
- [16] H. J. El-Khozondar and F. El-Batta, "Hybrid energy system for Dier El Balah quarantine center in Gaza Strip, Palestine," in *Proc. 2021 Int. Conf. on Electric Power Engineering – Palestine (ICEPE-P)*, Gaza, Palestine, 2021, pp. 1–6. <https://doi.org/10.1109/ICEPE-P51568.2021.9423489>
- [17] A. A. Z. Diab, H. M. Sultan, I. S. Mohamed, O. N. Kuznetsov, and T. D. Do, "Application of different optimization algorithms for optimal sizing of PV/Wind/Diesel/Battery storage stand-alone hybrid microgrid," *IEEE Access*, vol. 7, pp. 119223–119245, 2019. <https://doi.org/10.1109/ACCESS.2019.2936656>
- [18] M. A. Nyasapoh, S. K. Debrah, and D. K. Twerefou, "Long-term electricity generation analysis and policy implications – the case of Ghana," *Cogent Eng.*, vol. 10, no. 1, 2023. <https://doi.org/10.1080/23311916.2023.2209996>
- [19] G. A. James, F. S. Ahiabor, and E. M. Abalo, "Analysing the barriers to renewable energy adoption in Ghana using Delphi and a fuzzy synthetic evaluation approach," *Energy Sustain. Dev.*, vol. 85, p. 101667, 2025. <https://doi.org/10.1016/j.esd.2025.101667>

- [20] M. Sakah, F. A. Diawuo, R. Katzenbach, and S. Gyamfi, "Towards a sustainable electrification in Ghana: A review of renewable energy deployment policies," *Renew. Sustain. Energy Rev.*, vol. 79, pp. 544–557, 2017. <https://doi.org/10.1016/j.rser.2017.05.090>
- [21] European Union, "Directive 2009/28/EC of the European Parliament and of the Council of 23 April 2009 on the promotion of the use of energy from renewable sources," *Official J. Eur. Union*, no. 5, 2009.
- [22] A. Marina, S. Spoelstra, H. A. Zondag, and A. K. Wemmers, "An estimation of the European industrial heat pump market potential," *Renew. Sustain. Energy Rev.*, vol. 139, p. 110545, 2021. <https://doi.org/10.1016/j.rser.2020.110545>
- [23] V. Battaglia, L. Vanoli, C. Verde, P. Nithiarasu, and J. R. Searle, "Dynamic modelling of geothermal heat pump system coupled with positive-energy building," *Energy*, vol. 284, p. 126052, 2023. <https://doi.org/10.1016/j.energy.2023.126052>
- [24] H. Boughanmi, M. Lazaar, A. Farhat, and A. Guizani, "Evaluation of soil thermal potential under Tunisian climate using a new conic basket geothermal heat exchanger," *Appl. Therm. Eng.*, vol. 113, pp. 1455–1465, 2017. <https://doi.org/10.1016/j.applthermaleng.2016.10.204>
- [25] A. Allouhi, "Techno-economic and environmental accounting analyses of an innovative power-to-heat concept based on solar PV systems and a geothermal heat pump," *Renew. Energy*, vol. 191, pp. 649–661, 2022. <https://doi.org/10.1016/j.renene.2022.04.001>
- [26] D. A. Rodriguez-Alejandro et al., "Comprehensive analysis of a vertical ground-source heat pump for residential use in Mexico," *Geothermics*, vol. 99, p. 102300, 2022. <https://doi.org/10.1016/j.geothermics.2021.102300>
- [27] R. Saeidi, A. Karimi, and Y. Noorollahi, "The novel designs for increasing heat transfer in ground heat exchangers to improve geothermal heat pump efficiency," *Geothermics*, vol. 116, p. 102844, 2024. <https://doi.org/10.1016/j.geothermics.2023.102844>
- [28] H. M. Fouad, A. H. Mahmoud, and R. R. Moussa, "Effect of a geothermal heat pump system on cooling residential buildings in a hot, dry climate," *HBRC J.*, vol. 19, no. 1, pp. 483–507, 2023. <https://doi.org/10.1080/16874048.2023.2285095>
- [29] U. Acar and O. Kaska, "Performance assessments of ground source heat pump assisted by various solar panels to achieve zero energy buildings," *J. Build. Eng.*, vol. 96, p. 110611, 2024. <https://doi.org/10.1016/j.jobbe.2024.110611>
- [30] A. Ramos-Escudero, T. Magraner, and I. C. Gil-García, "Optimized spatial tool for the implementation of ground source heat pump coupled with photovoltaic panels heating systems in urban areas," *Energy Build.*, vol. 323, p. 114752, 2024. <https://doi.org/10.1016/j.enbuild.2024.114752>
- [31] K. Salhein et al., "Heat Transfer Performance Factors in a Vertical Ground Heat Exchanger for a Geothermal Heat Pump System," *Energies*, vol. 17, no. 19, p. 5003, 2024. <https://doi.org/10.3390/en17195003>
- [32] M. Vojdani, I. Fakhari, and P. Ahmadi, "A novel triple pressure HRSG integrated with MED/SOFC/GT for cogeneration of electricity and freshwater," *Energy Convers. Manage.*, vol. 233, p. 113876, 2021. <https://doi.org/10.1016/j.enconman.2021.113876>
- [33] J. Liu, S. Cao, X. Chen, H. Yang, and J. Peng, "Energy planning of renewable applications in high-rise residential buildings integrating battery and hydrogen vehicle storage," *Appl. Energy*, vol. 281, p. 116038, 2021. <https://doi.org/10.1016/j.apenergy.2020.116038>
- [34] M. Bortolini, M. Gamberi, and A. Graziani, "Technical and economic design of photovoltaic and battery energy storage system," *Energy Convers. Manage.*, vol. 86, pp. 81–92, 2014. <https://doi.org/10.1016/j.enconman.2014.04.089>

- [35] J. Neubauer and A. Pesaran, "The ability of battery second use strategies to impact plug-in electric vehicle prices," *J. Power Sources*, vol. 196, no. 23, pp. 10351–10358, 2011. <https://doi.org/10.1016/j.jpowsour.2011.06.053>
- [36] M. A. Cusenza et al., "Reuse of electric vehicle batteries in buildings," *Energy Build.*, vol. 186, pp. 339–354, 2019. <https://doi.org/10.1016/j.enbuild.2019.01.032>
- [37] S. B. Silva, M. M. Severino, and M. A. G. de Oliveira, "A stand-alone hybrid photovoltaic, fuel cell and battery system," *Renew. Energy*, vol. 57, pp. 384–389, 2013. <https://doi.org/10.1016/j.renene.2013.02.004>
- [38] A. Behzadi and A. Arabkoohsar, "Feasibility study of a smart building energy system," *Energy*, vol. 210, p. 118528, 2020. <https://doi.org/10.1016/j.energy.2020.118528>
- [39] X. Wang and M. Dennis, "Influencing factors on the energy saving performance of battery storage and phase change cold storage in a PV cooling system," *Energy Build.*, vol. 107, pp. 84–92, 2015. <https://doi.org/10.1016/j.enbuild.2015.08.008>
- [40] K. Karakoulidis et al., "Techno-economic analysis of a stand-alone hybrid photovoltaic-diesel-battery-fuel cell power system," *Renew. Energy*, vol. 36, no. 8, pp. 2238–2244, 2011. <https://doi.org/10.1016/j.renene.2010.12.003>
- [41] Y. Zhang, A. Lundblad, P. E. Campana, and J. Yan, "Comparative study of battery storage and hydrogen storage," *Energy Procedia*, vol. 103, pp. 268–273, 2016. <https://doi.org/10.1016/j.egypro.2016.11.284>
- [42] H. G. Ozcan et al., "Numerical simulation and parametric study of various operational factors," *Sustain. Cities Soc.*, vol. 67, p. 102754, 2021. <https://doi.org/10.1016/j.scs.2021.102754>
- [43] D. Boruah and S. S. Chandel, "A comprehensive analysis of eight rooftop grid-connected solar PV plants," *Sol. Energy*, vol. 266, p. 112154, 2023. <https://doi.org/10.1016/j.solener.2023.112154>
- [44] Z. Zhang, K. Wen, and W. Sun, "Optimization and sustainability analysis of a hybrid diesel-solar-battery system," *Sustain. Energy Technol. Assess.*, vol. 55, p. 102913, 2023. <https://doi.org/10.1016/j.seta.2022.102913>
- [45] R. Hemmati, "Dynamic expansion planning in active distribution grid," *Energy*, vol. 277, p. 127719, 2023. <https://doi.org/10.1016/j.energy.2023.127719>
- [46] K. Wang et al., "Emerging photo-integrated rechargeable aqueous zinc-ion batteries," *Carbon Neutralization*, vol. 2, no. 1, pp. 37–53, 2023. <https://doi.org/10.1002/cnl2.41>
- [47] J. Li, "Optimal sizing of grid-connected photovoltaic battery systems," *Renew. Energy*, vol. 136, pp. 1245–1254, 2019. <https://doi.org/10.1016/j.renene.2018.09.099>
- [48] W. L. Schram, I. Lampropoulos, and W. G. J. H. M. van Sark, "Photovoltaic systems coupled with batteries," *Appl. Energy*, vol. 223, pp. 69–81, 2018. <https://doi.org/10.1016/j.apenergy.2018.04.023>
- [49] O. Talent and H. Du, "Optimal sizing and energy scheduling of photovoltaic-battery systems," *Renew. Energy*, vol. 129, Part A, pp. 513–526, 2018. <https://doi.org/10.1016/j.renene.2018.06.009>
- [50] K. Solaun and E. Cerdá, "Climate change impacts on renewable energy generation," *Renew. Sustain. Energy Rev.*, vol. 116, p. 109415, 2019.
- [51] L. Shi and M. Y. L. Chew, "A review on sustainable design of renewable energy systems," *Renew. Sustain. Energy Rev.*, vol. 16, no. 1, pp. 192–207, 2012.
- [52] Rheem Manufacturing Company, *Heavy Duty Electric Water Heater Installation and Operating Manual*. Accessed Mar. 30, 2025. https://wholesalewaterheater.com/cdn/shop/files/Rheem_HeavyDuty_Electric_Manual.pdf?v=17347641233797743427

- [53] Bosch Thermotechnology, *WW Series, Bosch Home Comfort*. Accessed Mar. 30, 2025. <https://www.bosch-homecomfort.com/us/en/ocs/residential/ww-series-20078866-p>
- [54] One Building Energy Climate Data, “EnergyPlus weather data by region,” 2024. <https://climate.onebuilding.org/>
- [55] H. E. Beck, T. R. McVicar, N. Vergopalan, A. Berg, and E. F. Wood, “High-resolution (1 km) Köppen-Geiger maps for 1901–2099 based on constrained CMIP6 projections,” *Sci. Data*, vol. 10, p. 724, 2023. <https://doi.org/10.1038/s41597-023-02549-6>
- [56] S. Alkan and Y. Ates, “Pilot scheme conceptual analysis of rooftop East–West-oriented solar energy system with optimizer,” *Energies*, vol. 16, no. 5, p. 2396, 2023. <https://doi.org/10.3390/en16052396>
- [57] A. Malara, C. Marino, A. Nucara, M. Pietrafesa, F. Scopelliti, and G. Streva, “Energetic and economic analysis of shading effects on PV panels energy production,” *Int. J. Heat Technol.*, vol. 34, no. 3, pp. 465–472, 2016. <https://doi.org/10.18280/ijht.340316>
- [58] H. J. El-Khozondar, A. A. Asfour, Y. F. Nassar, S. W. Shaheen, M. F. El-Zaety, R. J. El-Khozondar, M. M. Khaleel, A. A. Ahmed, and A. H. Alsharif, “Photovoltaic solar energy for street lighting: A case study at Kuwaiti Roundabout, Gaza Strip, Palestine,” *Power Eng. Eng. Thermophys.*, vol. 3, no. 2, pp. 77–91, 2024. <https://doi.org/10.56578/peet030201>
- [59] Y. F. Nassar and A. A. Salem, “The reliability of the photovoltaic utilization in southern cities of Libya,” *Desalination*, vol. 209, pp. 86–90, 2007. <https://doi.org/10.1016/j.desal.2007.04.013>
- [60] Y. F. Nassar, H. J. El-Khozondar, S. Y. Alsadi, N. M. Abuhamoud, and G. M. Miskeen, “Atlas of PV Solar Systems Across Libyan Territory,” in *Proc. 2022 Int. Conf. on Engineering & MIS (ICEMIS)*, Istanbul, Turkey, 2022, pp. 1–6. <https://doi.org/10.1109/ICEMIS56295.2022.9914355>
- [61] Solar-Fabrik, “Mono S4 Halfcut | Trend White.” Accessed Mar. 30, 2025. <https://solar-fabrik.de/en/solar-modules/mono-s4-halfcut-trend-white/>
- [62] M. H. Abuqila, Y. F. Nassar, and M. A. Nyasapoh, “Estimation of the storage capacity of electric vehicle batteries under real weather and drive-mode conditions: A case study,” *Wadi Alshatti Univ. J. Pure Appl. Sci.*, vol. 3, no. 1, pp. 59–71, Jan.–Jun. 2025. https://doi.org/10.63318/waujpasv3i1_10
- [63] MG Solar Shop, “Cegasa eBick 280 PRO LiFePO4 battery extension 13.44 kWh,” MG Solar Shop. Accessed Mar. 30, 2025. <https://www.mg-solar-shop.com/cegasa-ebick-280-pro-lifepo4-battery-extension-13.44-kwh>
- [64] J. Claesson and P. Eskilson, “Conductive heat extraction to a deep borehole: Thermal analyses and dimensioning rules,” *Energy*, vol. 13, no. 6, pp. 509–527, 1988. [https://doi.org/10.1016/0360-5442\(88\)90005-9](https://doi.org/10.1016/0360-5442(88)90005-9)
- [65] M. Ahmadfard and M. Bernier, “A review of vertical ground heat exchanger sizing tools including an inter-model comparison,” *Renew. Sustain. Energy Rev.*, vol. 110, pp. 247–265, 2019. <https://doi.org/10.1016/j.rser.2019.04.045>
- [66] Grant Thornton, *Africa Renewable Energy Discount Rate Survey – 2018*, in collaboration with Renewables in Africa and Clean Energy Pipeline, Oct. 2018.
- [67] I. Dincer, M. A. Rosen, and P. Ahmadi, *Optimization of Energy Systems*. Hoboken, NJ, USA: Wiley, 2017.
- [68] S. M. Ahmad, A. Agrira, and Y. F. Nassar, “The impact of loss of power supply probability on design and performance of wind/pumped hydropower energy storage hybrid system,” *Wadi Alshatti University Journal of Pure and Applied Sciences*, vol. 3, no. 2, pp. 52–62, Jul.–Dec. 2025. https://doi.org/10.63318/waujpasv3i2_06

- [69] Republic of Tunisia, “Law No. 2015-12 of 11 May 2015 on the production of electricity from renewable energies,” *Official Gazette of the Republic of Tunisia*, no. 38, pp. 1243–1247, May 12, 2015.
- [70] K. Kusakana, “Optimal electricity cost minimization of a grid-interactive pumped hydro storage using ground water in a dynamic electricity pricing environment,” *Energy Reports*, vol. 5, pp. 159–169, 2019. <https://doi.org/10.1016/j.egy.2019.01.004>
- [71] M. Abdunnabi, N. Etiab, Y. F. Nassar, H. J. El-Khozondar, and R. Khargotra, “Energy savings strategy for the residential sector in Libya and its impacts on the global environment and the nation economy,” *Adv. Build. Energy Res.*, vol. 17, no. 4, pp. 379–411, 2023. <https://doi.org/10.1080/17512549.2023.2209094>
- [72] M. A. Eteriki, W. A. El-Osta, Y. F. Nassar, and H. J. El-Khozondar, “Effect of implementation of energy efficiency in residential sector in Libya,” in *Proc. 8th Int. Eng. Conf. on Renewable Energy & Sustainability (ieCRES)*, Gaza, Palestine, 2023, pp. 1–6. <https://doi.org/10.1109/ieCRES57315.2023.10209521>
- [73] G. N. B. Hendi, A. D. Zand, and M. R. Abyaneh, “Assessing the life-cycle greenhouse gas (GHG) emissions of renewable and fossil fuel energy sources in Iran,” *Environ. Energy Econ. Res.*, vol. 5, no. 2, pp. 1–9, 2021. <https://doi.org/10.22097/eeer.2021.258370.1176>
- [74] A. M. Makhzom, K. R. Aissa, A. A. Alshanokie, Y. F. Nassar, H. J. El-Khozondar, M. A. Salem, M. Khaleel, M. Bazina, and M. Elmnifi, “Carbon dioxide life cycle assessment of the energy industry sector in Libya: A case study,” *Int. J. Electr. Eng. Sustain.*, vol. 1, no. 3, pp. 145–163, Sep. 2023.
- [75] S. Malefaki, D. Markatos, A. Filippatos, and S. A. Pantelakis, “A comparative analysis of multi-criteria decision-making methods and normalization techniques in holistic sustainability assessment for engineering applications,” *Aerospace*, vol. 12, no. 2, p. 100, 2025. <https://doi.org/10.3390/aerospace12020100>
- [76] Y. F. Nassar, S. Y. Alsadi, H. J. El-Khozondar, and others, “Design of an isolated renewable hybrid energy system: a case study,” *Materials for Renewable and Sustainable Energy*, vol. 11, pp. 225–240, 2022. <https://doi.org/10.1007/s40243-022-00216-1>
- [77] U.S. International Trade Administration, *Tunisia – Electrical Power Systems and Renewable Energy*. <https://www.trade.gov/country-commercial-guides/tunisia-electrical-power-systems-and-renewable-energy>
- [78] E. Omri, N. Chtourou, and D. Bazin, “Solar thermal energy for sustainable development in Tunisia: The case of the PROSOL project,” *Renew. Sustain. Energy Rev.*, vol. 41, pp. 1312–1323, 2015. <https://doi.org/10.1016/j.rser.2014.09.023>